Pedro Manuel Oliveira Ventura

Licenciado em Biologia

Macrophages control tissue homeostasis via Ferritin heavy chain

Dissertação para obtenção do Grau de Mestre em
Genética Molecular e Biomedicina

Orientador: Prof. Dr. Miguel P. Soares, Investigador Principal no Instituto Gulbenkian da Ciência (IGC)

FACULDADE DE CIÊNCIAS E TECNOLOGIA
UNIVERSIDADE NOVA DE LISBOA

Setembro 2017

Macrophages control tissue homeostasis via Ferritin heavy chain

Declaration

The Master's candidate, Pedro Ventura, conducted his studies under the co-supervision of Dr. Miguel P. Soares, Dr. Birte Blankenhaus and Dr. Faouzi Braza at the Instituto Gulbenkian da Ciência, Oeiras. For this thesis entitled "Macrophage control tissue homeostasis via Ferritin heavy chain", the experimental work was performed by the candidate, Pedro Ventura, including analysis of the data and writing of the manuscript. Dr. Miguel P. Soares funded the project and supervised the work, including writing of the manuscript and the production of the figures. Dr. Birte Blankenhaus supervised the work, performed the real time PCR analysis, the experiments presented in Figure 3.3 and Figure 3.4 and developed along with Dr. Moises Mallo the CRISPR transgenic mice (V5-*Fth*) used in this thesis. Dr. Birte Blankenhaus also provided technical assistance with all the experiments using bone marrow chimeric mice, immunohistochemistry experiments and handling and crossing of the V5-*Fth* mice. Dr. Faouzi Braza supervised the work, writing of the manuscript and production of the figures as well as technical assistance for the immunohistochemistry and, along with Vasco Correia, splenectomy experiments. Dr. Ana Rita Carlos and Dr. Rui Martins provided guidance and assistance in the writing of the manuscript. Maria Raquel Moita provided technical assistance for experiments with western blots. Silvia Cardoso provided technical assistance with the handling and crossing of mice.

Index of contents

Index of figures

Index of tables

Acknowledgements

First and foremost I would like to thank Dr. Miguel P. Soares for giving me the opportunity to develop my Master thesis in his laboratory and for the important guidance he provided during the project. I also own a special thanks to Dr. Birte Blankenhaus and Dr. Faouzi Braza for their supervision, advice and patience in dealing with my inexperience. I want to give a special thanks to Dr. Moises Mallo for assisting Dr. Birte Blankenhaus in the development of the V5-*Fth* mice which were critical for my thesis. Next, I want to thank my colleges in the Inflammation laboratory for their kindness in accepting me as well as for their important assistance and cooperation in the lab and their friendship. Finally, I want to thank my family for their support, either financial or mostly importantly, emotional as well as my close friends and especially my girlfriend for her company, encouragement and care.

Summary

Due to its inherent capacity to catalyze reduction-oxidation reactions, iron is at the center stage of vital biological functions essential to most living organisms. Paradoxically, these same inherent characteristics are also responsible for the deleterious effects of iron. In the intracellular environment, iron is oxidized to its inert biological form by the ferroxidase activity of Ferritin Heavy Chain (FTH). In this Thesis we used a genetic loss of function approach in mice to demonstrate that FTH is essential to control the deleterious effects of iron and as such to maintain homeostasis *in vivo*. Namely we found that global deletion of the *Fth* allele is lethal in adult mice, an outcome prevented by the expression of FTH in macrophages. To investigate further the mechanisms by which FTH in macrophages contributes to maintain homeostasis we generated and characterized a genetically modified mouse strain in which FTH was tagged with a small V5 epitope. We found that contrary to what would be expected FTH is not secreted from macrophages to exert its protective effect. We conclude that FTH expression in macrophages acts in a cell autonomous manner to support homeostasis.

Keywords: Iron; FTH; Homeostasis; Macrophages.

Resumo

Devido à sua capacidade inerente em catalisar reações de oxidação-redução, o ferro desempenha um papel crítico em funções biológicas essenciais para a vida. Paradoxalmente, estas mesmas características são também responsáveis pelos efeitos nocivos do ferro. No ambiente intracelular o ferro é oxidado pela Ferritin Heavy Chain (FTH), tornando-o biologicamente inerte. Nesta tese, foi utilizada uma abordagem genética de perda-de-função em murganhos para demonstrar que FTH é essencial para controlar os efeitos nocivos do ferro e desta forma, sustentar a homeostasia *in vivo*. Nomeadamente, descobrimos que a deleção alélica global de *Fth* é letal em murganhos adultos e que este efeito é prevenido pela expressão de FTH em monócitos/macrófagos. Para investigar mais detalhadamente os mecanismos pelo qual a expressão de FTH em monócitos/macrófagos contribui para a manutenção da homeostasia gerámos e caracterizámos uma estirpe de murganhos geneticamente modificada em que FTH foi fundida com um pequeno epítopo V5. Ao contrário do que era esperado, foi descoberto que FTH não é secretada por monócitos/macrófagos para exercer o seu efeito protetor. Concluímos que a expressão de FTH em monócitos/macrófagos age de uma forma autónoma para suportar a homeostasia.

Termos-chave: Ferro; FTH; Homeostasia; Macrófagos.

1. Introduction

Iron (Fe) is one of the most abundant elements on earth and the most commonly used in reduction-oxidation (redox) reactions in virtually all living organisms (Aisen et al., 2001)(Gozzelino and Soares, 2014) (Figure 1.1). While the inherent capacity of Fe to catalyze redox reactions is used under physiologic conditions to support vital processes, such as energy production or oxygen transport and storage (MacKenzie et al., 2008; Wang and Pantopoulos, 2011), Fe can also promote the generation of free radicals via the Haber-Weiss and Fenton reactions (Gozzelino and Soares, 2014). The final step of this reaction (Fenton) occurs through the reaction of ferrous Fe (Fe^{2+}) with H_2O_2 which generates ferric Fe (Fe^{3+}), OH^- and hydroxyl radicals ($OH^{\cdot}$) (MacKenzie et al., 2008), which can cause lipid peroxidation, DNA damage/breaks or protein unfolding (Alkhateeb and Connor, 2013; Datz et al., 2017). This dual beneficial versus detrimental effect of Fe imposes an extremely delicate balance in the regulation of cellular/organismal Fe levels. Consequently, a set of tightly regulated mechanisms is needed to keep optimal Fe levels necessary for core biological function while preventing its cytotoxic effects.

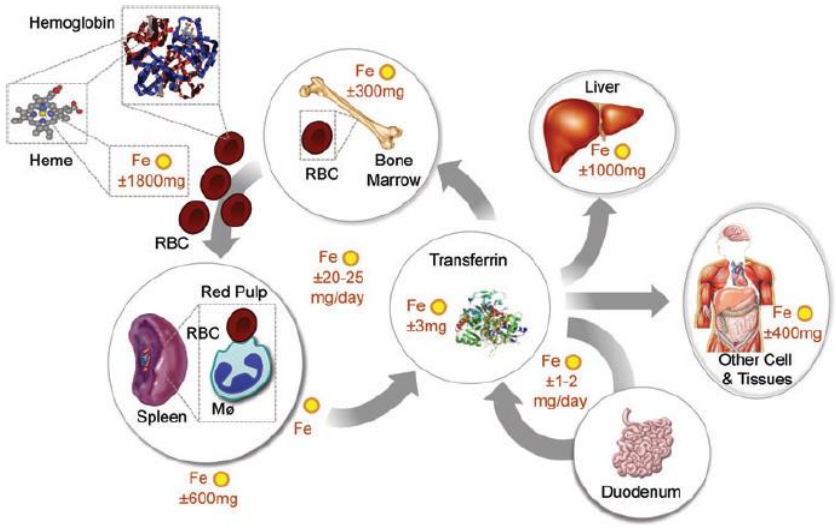

Figure 1.1. Systematic Fe distribution in mammals. Fe homeostasis involves a delicate balance between the Fe levels in different compartments. The Fe values in each box represent the total Fe content of each compartment and the arrows depict Fe movement across the several tissues. This movement is facilitated by transferrin, which is a plasma protein that acts as the main vehicle for Fe delivery to tissues. Because different tissues have distinct Fe requirements, the amounts of Fe vary greatly across tissues. The majority of Fe is located within the heme moiety of hemoglobin in RBCs (RBC). The liver serves as a Fe storage compartment, and as such takes up a significant amount of Fe, while the bone marrow and the spleen account for the bulk of the Fe being recycled and utilized for erythropoiesis. Accordingly, around 20-25 mg of Fe are used for physiological functions each day. Intestinal Fe absorption of Fe is minimal, and accounts for just 1-2 mg of Fe a day, a small proportion of the daily Fe requirements of the organism. Taken from (Gozzelino and Soares, 2014).

In mammals, around 65-70% of Fe is contained in heme (Frazer and Anderson, 2014), a prosthetic component of hemoglobin, myoglobin and cytochromes (Gozzelino et al., 2010; Gozzelino and Soares, 2014). Approximately 20% of the remaining Fe is stored by macrophages and hepatocytes with 10-15% being constantly utilized for cellular functions (Frazer and Anderson, 2014). Given that Fe is utilized at a faster rate than it is taken up from diet, systemic Fe levels are actively maintained through recycling mechanisms that involve the re-utilization of the Fe stores contained in senescent red blood cells (RBC) (Gozzelino and Soares, 2014)(Soares and Hamza, 2016). Nevertheless, systemic Fe homeostasis relies on continuous Fe uptake from diet, needed to compensate for Fe losses through epithelial desquamation, sweat or blood loss (Hentze et al., 2010). Fe uptake from diet occurs predominantly on the intestinal lumen at the level of the duodenum and upper jejunum, being absorbed essentially as non-heme Fe (90%) (Muñoz et al., 2011; Wang and Pantopoulos, 2011). Fe is absorbed in the form of Fe^{3+} and is reduced by duodenal cytochrome B (DCYTB) reductase into Ferrous iron (Fe^{2+}) in the apical membrane of enterocytes (Vanoaica et al., 2010) (Figure 1.2). Fe is then imported by enterocytes by the divalent metal transporter 1 (DMT-1) (Vanoaica et al., 2010) (Figure 1.2) and either stored by intracellular ferritin (Vanoaica et al., 2010) or exported by ferroportin 1 (FPN; solute carrier family 40 member 1; SLC40A1), a transmembrane protein expressed in the basolateral membrane of enterocytes (MacKenzie et al., 2008) (Figure 1.2). To be exported, Fe^{2+} needs to be oxidized into Fe^{3+}, via a reaction catalyzed by hephaestin (HEPH), located in the enterocyte plasma membrane in close vicinity to FPN (Muckenthaler et al., 2017). Extracellular Fe^{3+} binds with remarkably high affinity to the plasma transferrin (TF) (Anderson et al., 2012)(Wang and Pantopoulos, 2011). Circulating TF-Fe complexes are bound by the transmembrane Fe transporters transferrin receptor 1 and 2 (TFR-1 and TFR-2) and internalized, via endocytosis, in a variety of cell types. Within the endo-lysosomal compartment, Fe is released from TF via a process that requires lysosomal acidification. This decreases TF affinity towards Fe^{3+}, allowing its release into the endosomal lumen (Wang and Pantopoulos, 2011). Upon release,

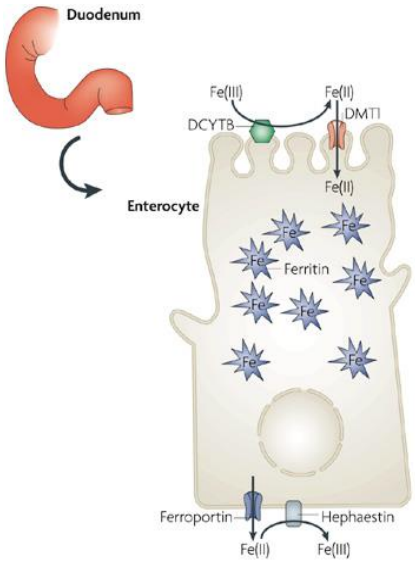

Figure 1.2 Intestinal Fe uptake. Simplified scheme illustrating dietary Fe absorption through the apical side of enterocytes in the duodenum and the major players involved in the transport of Fe to systemic circulation. Fe (III) represents ferric Fe which is reduced by DCYTB to ferrous Fe represented in the figure as Fe (II). Fe (II) can be taken up by enterocytes though DMT1 and according to physiological Fe needs, can be stored in Ferritin or exported into circulation through Ferroportin in the basal side. Fe (II) is then converted into Fe (III) by Hephaestin so that it can be posteriorly bound to transferrin and enter circulation. Taken and adapted from (De Domenico et al., 2008).

Fe^{3+} is reduced by metalloreductases, such as the six-transmembrane epithelial antigen of prostate family member 3 (STEAP-3) (Hentze et al., 2010) and transported to the cytoplasm by DMT-1 (Frazer and Anderson, 2014) where it can be used by cells, for example in the heme biosynthetic pathway but also in other biological processes.

Plasma Fe levels are regulated systemically by hepcidin, an acute phase protein produced mainly by hepatocytes and secreted into the blood stream (Ganz and Nemeth, 2015) (Figure 1.3). Hepcidin expression is itself regulated by a feedback mechanism loop that is sensitive to Fe concentration in the plasma or in the liver and that responds to erythropoietic Fe demand (Ganz, 2011). Namely, hepcidin is produced and released systemically in response to high Fe concentration in plasma and mediates systemically the internalization and subsequent degradation of FPN. This suppresses cellular Fe export, therefore promoting intracellular Fe retention by ferritin (Frazer and Anderson, 2014). When Fe concentration in plasma decreases, hepcidin production is suppressed, allowing for FPN expression and cellular Fe release/export into plasma (Frazer and Anderson, 2014). More recently, decrease levels of erythropoiesis have also been shown to inhibit hepcidin production through the release of erythroferrone (Kautz et al., 2014).

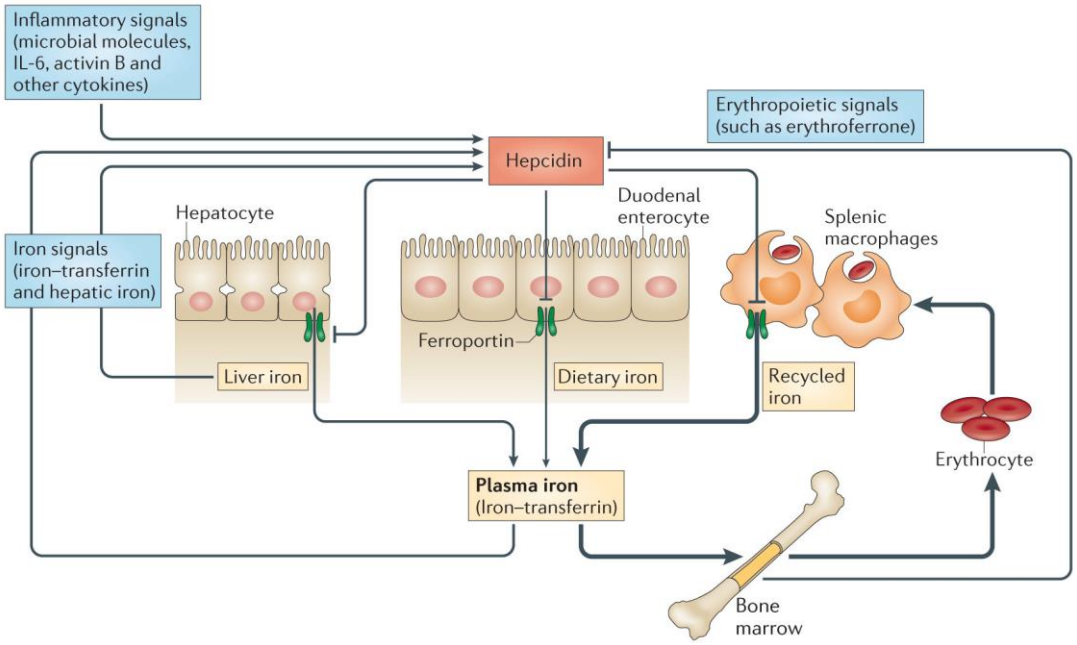

Figure 1.3. Hepcidin regulates Fe homeostasis systemically. In response to excessive Fe levels and inflammatory cues such as microbial peptides, IL-6, activin B and other inflammatory cytokines, hepcidin production in the liver increases. Hepatocytes produce and secrete the Fe hormonal regulator hepcidin, which acts systematically by being released into circulation and inducing ferroportin degradation thus promoting intracellular Fe retention. This effect inhibits ferroportin expression on a wide range of cells such duodenal enterocytes, splenic macrophages and hepatocytes which in turn reduces levels of plasma Fe bound to transferrin. This can lead to decreased levels of erythropoiesis prompting the release of erythroferrone from the bone marrow that inhibits hepcidin production. Taken from (Ganz and Nemeth, 2015).

Although systemic Fe levels are regulated mostly by hepcidin, it is also important to control Fe intracellular levels. This is achieved by the iron regulatory elements/iron regulatory proteins (IRE/IRP) machinery (Frazer and Anderson, 2014; Wilkinson and Pantopoulos, 2014), acting essentially at a post-transcriptional level to regulate the expression of proteins controlling cellular Fe metabolism. Briefly, this is mediated by the interaction of iron binding proteins 1 and 2 (IRP1 and IRP2) with specific conserved cis-regulatory stem-loops present in the mRNA sequence of Fe-responsive genes, termed iron responsive elements (IREs) (Frazer and Anderson, 2014; Gozzelino and Soares, 2014). IRPs are cytosolic proteins that bind to IRE sequences present in 5' and 3' untranslated regions (UTR) on the mRNA of several proteins responsible for the maintenance of Fe homeostasis such as TFR-1, DMT-1, ferritin H chain (FTH), ferritin L chain (FTL) and FPN (177). Although each IRP protein binds to IRE sequences with similar affinity, each IRP is regulated in a different manner (Wilkinson and Pantopoulos, 2014). When cellular Fe concentration is high, IRP-1 sequesters Fe, which forms an Fe-sulfur cluster (Anderson et al., 2012) that has the ability to act like a molecular switch preventing IRP-1 from binding to IRE motifs (Wilkinson and Pantopoulos, 2014). Conversely, when Fe concentration becomes limiting, the Fe-sulfur cluster becomes unstable and breaks down causing a conformational change that enables binding to the IREs (Frazer and Anderson, 2014). IRP-2 does not contain a Fe-sulfur cluster and can bind constitutively to IREs, when Fe level are low (Anderson et al., 2012). However, when intracellular Fe concentration increases, IRP-2 is degraded by an Fe-dependent ubiquitin-ligase called SKP1-CUL1-F-box (SCF), leading to proteasomal degradation (Frazer and Anderson, 2014). Depending on the cellular Fe requirements, IRPs can have opposite effects on the stability of the mRNA of different Fe-responsive proteins, hence regulating their expression and function (Frazer and Anderson, 2014). This process is pivotal in the cellular Fe acquisition avoiding its cytotoxic effects while maintaining Fe availability to support vital biologic functions (Anderson et al., 2012). This is perhaps best illustrated for the regulation of FTH and TFR-1 (Figure 1.4). Namely, when cellular Fe levels are low, IRP-1 and IRP-2 are actively bound to five IRE motifs in the 3' UTR region of *Tfr-1* mRNA promoting its stabilization and allowing for increased levels of protein expression and subsequently favoring cellular Fe internalization (Muckenthaler et al., 2017). On the other hand, IRP-1 and IRP-2 bound to the sole IRE motif in the 5' UTR region of *Fth* mRNA inhibit its translation by preventing ribosome attachment (Hentze et al., 2010; Arosio et al., 2017). This antithetical effect allows for Fe uptake by TFR-1 when cellular Fe concentration is low while concurrently inhibiting ferritin production (Wilkinson and Pantopoulos, 2014) (Figure 1.4). The reverse happens when cellular Fe concentration is high, as the cell shuts down Fe import by inhibiting TFR-1 while increasing cellular Fe storage (Muckenthaler et al., 2017).

The majority of bioavailable Fe is contained in the form of heme, the prosthetic group contained in hemoglobin, myoglobin and cytochromes as well as other hemoproteins (Gozzelino

et al., 2010) (Figure 1.5). About 20-25 mg of Fe is needed by the bone marrow per day for the de novo synthesis of the heme required to generate hemoglobin (Ganz, 2012) (Figure 1.5). By contrast, Fe uptake from diet only accounts for 1-2 mg on a daily basis (Gozzelino and Soares, 2014). In adult humans, around 200 billion of RBCs are produced each day which requires an extraordinary $2x10^{15}$ Fe atoms to be used per second (Muckenthaler et al., 2017). Each erythrocyte contains approximately 1.2×10^{9} of heme molecules associated with hemoglobin, and approximately 200 billion erythrocytes become senescent every day (Muckenthaler et al., 2017).

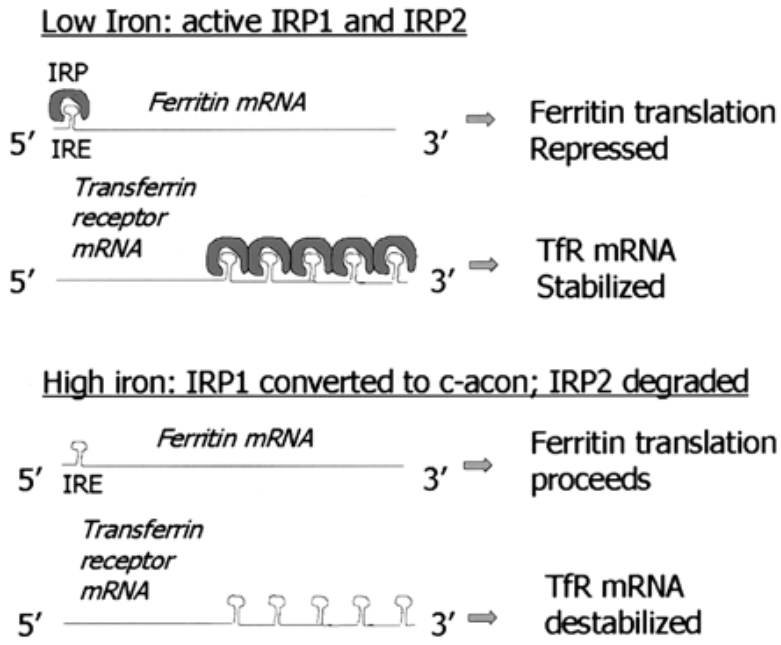

Figure 1.4 IRP/IRE machinery controls intracellular Fe responses. In response to low iron levels, IRP-1 and IRP-2 become activated and are able to bind to IRE sequences in the 5' and 3' end of FTH and Transferrin Receptor (TfR) respectively which inhibits translation of both ferritin subunits while promoting iron uptake by increasing TfR mRNA stability and subsequent translation. In an excessive intracellular environment IRP-1 forms an iron sulfur cluster and acts like a cytosolic aconitase (c-acon) redering it unable to interact with IREs while IRP-2 is degraded making it uncapable of binding to IREs, thus promoting iron storage by increasing ferritin mRNAs translation and inhibiting iron uptake by destabilizing TfR mRNA. Taken from (Torti and Torti, 2002).

Damaged or aged erythrocytes can leak hemoglobin into the circulation, which upon loss of conformational stability, release their heme moiety potentiating generation of lipid peroxides, damage to DNA and oxidative damage of proteins (Alkhateeb and Connor, 2013). Additionally, Fe released from heme can further generate deleterious free radicals *via* the Fenton reaction (Nairz et al., 2017). Just a small release of the potentially cytotoxic labile Fe contained in hemoglobin can generate extensive damage and argues for the necessity of tightly controlled regulatory mechanisms that efficiently recycle and distribute Fe throughout the organism (Soares and Hamza, 2016).

In order to avoid widespread Fe-driven oxidative damage, several protective programs are in place. At steady state, damaged and senescent erythrocytes are detected by erythrophagocytic macrophage subsets which reside in the spleen, liver, and bone marrow. These erythrophagocytic macrophages that engulf and digest senescent or damaged erythrocytes, actively prevent the development of heme-Fe stress and damage. In the spleen, erythrophagocytosis is primarily achieved by Red-Pulp Macrophages (RPMs) which express scavenger receptors (Nairz et al., 2017) allowing phagocytosis and internalization of the RBCs (Soares and Hamza, 2016). After internalization, heme is catabolized in the phagolysosome of RPMs and subsequently transported to the cytoplasm via the heme-responsive gene 1 (HRG-1) (Soares and Hamza, 2016). This leads to the accumulation of labile heme in the cytoplasm which results in the induction of heme oxygenase 1 (HO-1) expression (Gozzelino et al., 2010). This catabolizes heme , generating equimolar amounts of carbon monoxide (CO), biliverdin and Fe^{2+} (Gozzelino et al., 2010). Then, depending on the systemic Fe equilibrium, the released Fe^{2+} can be either stored inside the cell by incorporation into ferritin or exported via FPN-1 (Frazer and Anderson, 2014). Once exported, Fe binds TF to form TF-Fe complexes (Nairz et al., 2017), which can be further utilized for *de novo* hemoglobin synthesis by erythroblasts during erythrocyte development.

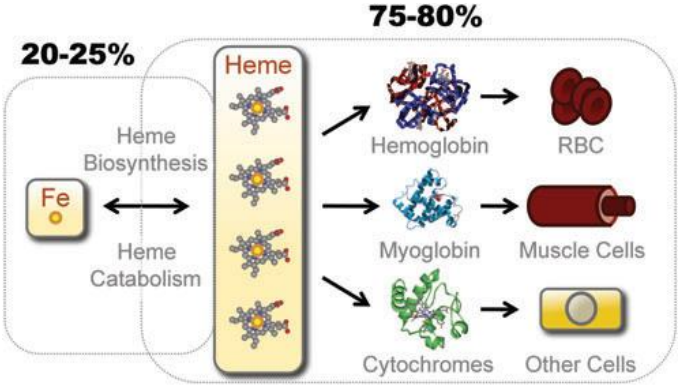

Figure 1.5. Bioavailable Fe in mammals. Considering the totality of bioavailable Fe in mammals, only 20-25% is associated with Fe binding proteins, the rest is associated with heme-containing molecules such as hemoglobin, myoglobin and cytochromes which are the main hemoprotein compartments in mammals. Hemoglobin is abundantly present in red blood cells (RBCs), myoglobin in muscle cells and cytochromes in the majority of other cells. Distribution inside each of these compartments is also considerably unequal since 70% of this heme is contained in hemoglobin while the remaining 20-25% and 5-10% are contained in cytochromes and myoglobin respectively. Fe can transit from heme to non-heme or conversely through *de novo* heme catabolism or biosynthesis. Taken from (Gozzelino and Soares, 2014).

Differentiation of RPMs in the spleen is dependent on the expression of the transcription factor SPI-C (Kierdorf et al., 2016), as the deletion of SPI-C prevents the generation of RPMs and alters the formation of the red pulp in the spleen (Kohyama et al., 2009; Nairz et al., 2017). Furthermore, heme leads to the induction of SPI-C (Haldar et al., 2014) via the binding to a repressor called Btb and Cnc Homology 1 (BACH-1) that constitutively inhibits SPI-C expression (Haldar et al., 2014). Binding of heme to BACH1 triggers its degradation allowing for expression of SPI-C and differentiation of RPMs (Kurotaki et al., 2015). Although it remains unknown whether this pathway is active during fetal development of macrophages**,** hemolytic diseases leading to splenic heme overload drive the expression of SPI-C in circulating monocytes that then migrate to the

spleen and help prevent heme-Fe-related cytotoxicity by providing a functional support to RPMs (Haldar et al., 2014). A very similar mechanism has been described whereby heme-Fe accumulation in the liver drives the differentiation of circulating monocytes into a functional Fe-recycling macrophage subset that expresses high levels of FPN (Theurl et al., 2016). Similarly, acute kidney failure induced by accumulation of myoglobin after muscle injury, drives the recruitment and differentiation of macrophages which then can activate the expression of HO-1 (encoded by *Hmox1*) as well as the expression of CD163 and ferritin to detoxify heme-Fe (Nairz et al., 2017). Macrophages also play an important role in Fe clearance in the heart, an organ known to be extremely sensitive to Fe-induced toxicity due to the lack of regenerative potential of the myocardium (Nairz et al., 2017). In fact, these cell types have been shown to provide Fe for the myocardium and detoxify heme-Fe preventing tissue injury (Nahrendorf and Swirski, 2016). Moreover, a recent study showed that the recruitment of macrophages to sites of muscle damage is essential to promote muscle tissue regeneration while preventing Fe-associated cytotoxicity (Corna et al., 2016). After acute muscle injury and release of myoglobin, muscle-infiltrating macrophages not only take up Fe to prevent tissue damage but also promote regeneration and proliferation of muscle stem cells through a mechanism involving FPN-mediated Fe export (Corna et al., 2016). Finally, macrophages developed several mechanisms that enable them to clear or resolve Fe overload and return to steady-state conditions. One such strategy is through the incorporation of Fe in ferritin which can act as a mechanism to detoxify Fe mediated cytotoxicity and prevent tissue Fe overload (Theil, 2013; Nairz et al., 2017). Interestingly, macrophages express high levels of ferritin that is secreted into plasma

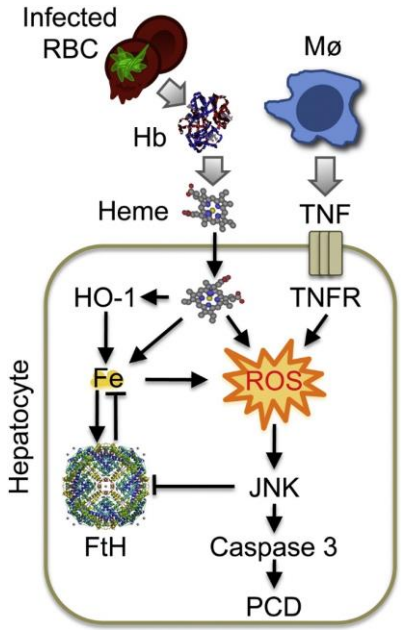

Figure 1.6. Salutary effects of ferritin in the overall reduction of reactive oxygen species. Disruptions in Fe homeostasis caused by hemolysis, infection or inflammatory cues such as release of Tumor Necrosis Factor (TNF) by macrophages cause an overall increase in intracellular reactive oxygen species (ROS) levels. TNF (internalized by the TNF receptor, TNFR) can directly generate ROS while heme can act directly or indirectly after release of Fe by increasing the labile Fe pool. The synergistic effect of these molecules leads to constant high concentrations of ROS that sustain the activation of c-Jun N-terminal kinase (JNK) signaling transduction pathway that inhibits FTH synthesis and leads to the activation of Caspase 3 which culminates in programed cell death (PCD). The ferroxidase activity of FTH counteracts the accumulation of ROS by retaining Fe in a non-reactive form thus preventing potential intracellular labile Fe accumulation, which ultimately prevents cell death. Adapted from (Gozzelino et al., 2012).

(Cohen et al., 2010). The secreted ferritin can act as an Fe source for erythroid progenitor cells (Leimberg et al., 2008), suggesting that macrophage-derived ferritin functions as vehicle for Fe transport/transit (Leimberg et al., 2008) providing Fe to tissues in a non-cytotoxic form.

In animals, ferritin is composed of a highly conserved ferritin Heavy chain (FTH) and ferritin Light chain (FTL). The two proteins self-assemble and organize into a multimeric complex of 24 subunits, giving rise to a 480 kDa hollow sphere (Arosio et al., 2017). This complex is capable of storing up to 4500 atoms of Fe^{3+} (Arosio et al., 2015), an effect that relies on the ferroxidase activity of FTH, which converts highly reactive Fe^{2+} into Fe^{3+} thereby inhibiting the production of free radicals via the Fenton reaction (Gozzelino and Soares, 2014; Arosio et al., 2015). The FTL subunit does not possess ferroxidase activity, and is instead responsible for the formation of the Fe core inside the protein shell (Arosio et al., 2017).

Ferritin expression is regulated by several molecular pathways which act both at the transcriptional and post-transcriptional level (Theil, 2013; Wilkinson and Pantopoulos, 2014). Transcriptional regulation occurs mainly through the activation of nuclear factor kappa B (NF-kB) and the transcription of nuclear factor E2-related factor-2 (NRF2) (Gozzelino and Soares, 2014) as well as BACH1-1 which is a transcriptional regulator of the macrophage lineage (Soares and Hamza, 2016). As mentioned above, ferritin regulation also occurs post-transcriptionally via the IRP/IRE machinery, allowing for quick and efficient responses up-regulating ferritin when Fe levels are high and inhibiting its expression when Fe levels are low (Torti and Torti, 2002).

These observations have placed ferritin regulation not only in the context of Fe homeostasis but also in the broader framework of cell injury, oxidative stress and inflammation (Torti and Torti, 2002) (Figure 1.7). The imbalances and disruptions that occur in cellular Fe and ferritin levels are emerging as an important element in the pathogenesis of several diseases (Theil, 2013; Papanikolaou and Pantopoulos, 2017). Interestingly, while mutations in the FTL subunit can lead to a wide range of Fe related pathologies (Finazzi and Arosio, 2014) no mutations in the coding sequence of *Fth* are known, arguing for the incompatibility of life in the absence of this protein (Finazzi and Arosio, 2014). Deletion of the *Fth* allele is embryonic lethal in mice whereas the sole expression of FTL is unable to maintain Fe in a non-toxic form and compensate for the absence of FTH (Ferreira et al., 2000). Additionally, conditional deletion of *Fth* leads to the loss of intracellular Fe storage capacity and to tissue damage in the liver (Darshan et al., 2009) while *Fth* deletion in tubular kidney cells leads to renal inflammation through the influx and accumulation of macrophages with a dysregulated polarization profile (Bolisetty et al., 2015).

Outline of the master project

Given that deletion of *Fth* allele is embryonically lethal in mice the host laboratory developed a mouse strain that allows for regulated *Fth* allele deletion in adult animals. Unexpectedly, *Fth* deletion led to multi-organ dysfunction and death. This outcome was avoided when *Fth*-deleted mice were transplanted with wild-type bone marrows (See the "Results" section), an effect that relies on the expression of *Fth* in the monocytic lineage. My research project focused on addressing three main questions. First, what is the contribution of FTH expression by macrophages to FTH expression by parenchyma tissues? Second, what macrophage population is involved in maintenance of Fe homeostasis via the expression of FTH? Third, can macrophages deliver FTH directly to parenchyma tissues? The data obtained suggest that: i) FTH expression by macrophages contributes critically to the overall expression of FTH in parenchyma tissues, ii) Bone marrow derived $Ccr2^{+}$ macrophages are likely involved in maintenance of Fe homeostasis via the expression of FTH and iii) Macrophages do not deliver FTH directly into cells from parenchyma tissues.

2. Materials and Methods

2.1. Mice

The following mouse strains developed in the host laboratory were used for this Master thesis project:

Table 2.1. Experimental organisms used in this thesis, along with their original sources and references.

Organism/Strain	Reference	Source
C57BL/6J	*Charles River Laboratories*	*N/A*
B6. Fth$^{lox/lox}$	(Darshan et al., 2009)	*Prof. Lukas Kuhn, ETH, Switzerland*
B6.ROSA26$^{Cre-ERT2}$	(Vooijs et al., 2001)	JAX stock 008463
B6.ROSA26$^{Cre-ERT2}$ Fth$^{lox/lox}$	(Weis, Carlos et al., 2017)	*IGC*
B6.*LyzM^{Cre}Fth$^{Δ/Δ}$*	(Weis, Carlos et al., 2017)	*IGC*
B6.CX$_3$CR1$^{CreER-EYFP}$R26$^{DsRedfl/fl}$Fth$^{lox/lox}$	*Unpublished*	*IGC*
B6.CCR2$^{-/-}$	(Boring et al., 1997)	JAX stock 004999
B6.*V5-Fth*	Unpublished	*IGC*

Every procedure involving animals was performed in compliance with institutional and national guidelines. All animal protocols used were approved by the Instituto Gulbenkian de Ciência ethical committee and the ‘‘Órgão Responsável pelo Bem-estar dos Animais (ORBEA)’’ and consequently licenced by the Direccão Geral de Alimentação e Veterinária (DGAV). All animal experiments follow the Portuguese (Portaria nº 1005/92, Decreto-Lei nº 113/2013) and European (Directive 2010/63/EU) legislations, concerning housing, husbandry and animal welfare.

2.1.1. Allele deletion

Deletion of floxed alleles by Cre recombinase activation was achieved by Tamoxifen administration (Sigma-Aldrich Ref: T5648-5G). For deletion of *R26*$^{CreER-T2}$*Fth*$^{lox/lox}$ mice a stock solution of 45mg/mL of Tamoxifen in 5% EtOH/Corn oil was prepared and sonicated for 5min (60W). For the deletion of bone marrow chimeric mice a stock solution of 10mg/mL of Tamoxifen in 5% EtOH/Corn oil was prepared, sonicated for 5 min (60W), and vortexed (1 min) and 100μL Tamoxifen solution (1mg) was administered by oral gavage 3 times every other day. For deletion of *CX$_3$CR1$^{CreER-EYFP}$R26$^{DsRedfl/fl}$Fth$^{lox/lox}$* (henceforth referred as Cx3cr1$^{CreER-T2}$*Fth*$^{lox/lox}$) mice, Tamoxifen was administered by oral gavage 9 times, twice a week, or alternatively using Tamoxifen enriched diet (360 mg/kg Tamoxifen citrate Ssniff Spezialdiäten Ref: A115T70360), 2 times per week, every other week.

2.2. Bone marrow chimeric mice

2.2.1. Irradiation

Recipient mice were lethally irradiated (750 rads) by exposure to a Cesium radioactive source (3 min) in a Gamma Cell 2000 irradiator (Molsgaard Medical Serial Number: 86/4/14).

2.2.2. Bone marrow extraction and cell isolation

Bone marrow donor mice were sacrificed by CO_2 narcosis until a complete heart arrest was reached. The tibia and femur bones were isolated and placed in ice cold RPMI 1640 Medium, GlutaMAX supplement (Thermo Fisher Ref: 61870-010). Bones were cut and the bone marrow was flushed using a 10 mL syringe (Terumo Ref: SS+10ES1) with a 0,5x16 mm 25G x 5/8 disposable needle (Poulten John LTD Ref: 7.510-02). Cells were washed two times in RPMI at (Eppendorf Centrifuge 5810R) (4ºC 10 min, 300 g). Cells were re-suspended in 10 mL RPMI and subsequently passed through 100 μm cell strainers (BD Biosciences Ref: 352360). Cell number was quantified in a hemocytometer with a Trypan Blue solution (Sigma Ref: T8154). After quantification, cells were centrifuged again at 4ºC for 10 mins at 300 g and subsequently re-suspended in an adequate volume of PBS required for a cell suspension of $2.5x10^7$ /mL.

2.2.3. Bone marrow chimeric mice

After quantification, cells were re-suspended in Phosphate-Buffered Saline (PBS) ($2.5x10^7$ cells mL^{-1}). $5x10^6$ hematopoietic cells were intravenously injected in the tail of lethally irradiated recipient mice. Cells were allowed to engraft the recipient mice bone marrow and immune cell reconstitution was analyzed in blood by flow cytometry after 8 weeks. An irradiation control mouse was used that did not receive bone marrow after lethal irradiation.

2.2.4. Bone marrow reconstitution check by Flow Cytometry

8 weeks after bone marrow reconstitution, blood was collected from the tail and placed in (PBS). The cells were pelleted after centrifugation at 4ºC (Eppendorf Centrifuge 5810R) for 5 min, 300 g. Supernatant was discarded followed by incubation with erythrocyte lysis buffer (5 min) to lyse red blood cells (90% 160 mM Ammonium Chloride; 10% 100 mM Tris-HCl). Between each incubation step the cells were washed with PBS. Afterwards, the cells were stained with Fc Block (ref) for 15 min at 4ºC and labeled with lineage specific Abs (see 2.2.5 Abs for flow cytometry) for 30 min at 4ºC in the dark. Non-bound Abs were washed and the cells re-suspended in PBS.

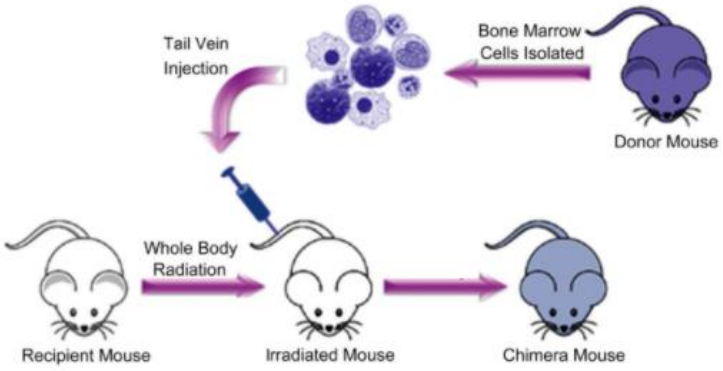

Figure 2.1. Schematic representation of the generation of bone marrow chimeric mice. Radiation was performed with 750 rad. Mice were left to recover for 8 weeks to allow for full reconstitution of the host immune system. Taken and adapted from (Ravikumar et al., 2014).

2.2.5. Abs for flow cytometry

Cells were labeled according to cell surface lineage markers that allowed identification of distinct cell types. For identification of B cells, they were labeled with anti-CD19 Ab conjugated with the fluorophore PECy7, for T cells the labelling was done with anti- TCR-b Ab conjugated with Bv421 fluorophore, for monocytes identification was achieved by labeling with anti-CD11b Ab conjugated with PerCpCy5.5 fluorophore and for neutrophils the staining was performed with both anti-CD11b conjugated with PerCpCy5.5 and Ly-6G/Gr1 conjugated with PE Abs. All Abs used were kept at 4º C and protected from light to avoid fluorophore photo-bleaching. For Ab isotype and references check Table 2.2.

Table 2.2. Abs used for flow cytometry experiments, along with the sources and references.

Cell Type	Ab	Isotype	Source	Reference
B Cells	PE/Cy7 anti-mouse CD19	Rat IgG2a, κ	Biolegend	115520
T cells	Brilliant Violet 421™ anti-mouse TCR β chain	Armenian Hamster IgG	Biolegend	109230
Monocytes	PerCP/Cy5.5 anti-mouse/human CD11b	Rat IgG2b, κ	Biolegend	101228
Neutrophils	PE Rat Anti-Mouse Ly-6G	Rat IgG2a, κ	BDBiosciences	551461

2.2.6. Cell staining acquisition

Flow cytometry acquisition was performed immediately after reconstitution check and acquired in Fortessa X20 (BD Biosciences). 10,000 cells were counted per sample and the data was analyzed on FlowJo VX (Tree Star Inc, Country).

2.3. Genotyping

2.3.1. Deoxyribonucleic acid (DNA) extraction

A piece of tail from each mouse was extracted and placed in individual Eppendorf tubes. Fresh KAPA Mouse Genotyping Kit extraction enzyme and extraction buffer (Kapa Biosystems Ref: KK7352), and ultrapure water was added to each tube in the following amounts (1x volume for a total volume of 50 μL/tube): 1 μL Extraction enzyme, 5 μL Extraction buffer, 44 μL ultrapure water. Samples were incubated at 75ºC in a hot plate for 15 min and afterwards at 95ºC for 5 min. Samples were quickly vortexed for 5 seconds and centrifuged for 1 min at room temperature in an Eppendorf Centrifuge 5415D. From this point, samples can be stored at -20ºC or -80ºC for optimal preservation of the extracted DNA.

2.3.2. Polymerase Chain Reaction (PCR)

For the PCR reaction the extracted DNA was added to a master mix prepared from KAPA Mouse Genotyping Kit (Kapa Biosystems Ref: KK7352) by combining the following components. (1x volume for a total volume of 10 μL/tube): 5 μL 2x KAPA 2G Fast genotyping mix; 0,5 μL Forward primer; 0,5

μL Reverse primer; 3 μL ultrapure water; 1 μL DNA sample. All PCR reactions were performed using a MyCycler™ Thermal Cycler System (BIO-RAD Ref: 1709703) using the following program:

- 95ºC – 5 min
- 95ºC – 15 seconds
- Tm – 15 seconds
- 72ºC – 20 seconds

35 cycles

- 72ºC – 5 min
- 4ºC – 60 min

Different annealing temperatures (Tm) were used depending on the specific screening. The different primers are indicated in Table 2.3.

Table 2.3. PCR primers used and experimental conditions. *Fwd* stands for Forward primer and *Rev* stands for Reverse primer.

Target gene	Primers (5'→3')	Size (bp)	Annealing
Fth	*Fwd*- CCAGAGTCGCCGCGGTTTCC *Rev*- GGTTGATCTGGCGGTTGATGG	233	69ºC
V5-Fth	*V5-Fwd*- ATGACCGGCAAGCCCATCC *Rev*- GGTTGATCTGGCGGTTGATGG	167	66ºC

2.3.3. Gel electrophoresis

Electrophoresis 1.5% agarose gel was prepared using the following components (for 150mL of total volume):

- Agarose (Lonza Verviers Ref: 50004) - 2,25 gr
- (Tris-Acetate) TAE buffer 1x (40 mM Tris, 20 mM acetic acid and 1 mM EDTA) - 150 mL
- RedSafe Nucleic Acid Staining Solution (INTRON Ref: 21141) - 15 μL

Agarose and TAE buffer were mixed and heated on a normal kitchen microwave for 3 min until boiling. After the agarose completely dissolved the RedSafe Nucleic Acid Staining Solution was added in the previous indicated amount. The gel was allowed to solidify for 30 min at room temperature. PCR products were added to each well alongside a Gene Ruler 100bp DNA Ladder (Thermo Scientific Ref: SM0241). Electrophoresis was performed in a Sub-Cell® GT Agarose Gel Electrophoresis Systems

(BIO-RAD) gel chamber filled with 1x TAE buffer at a constant voltage of 80-100V for 30-60 min. Results were analyzed by UV radiation in a Gel Doc EZ Imager (BIO-RAD Ref: 170-8270).

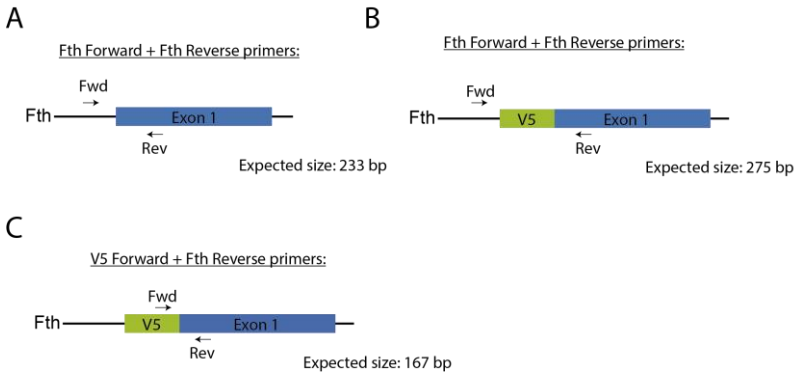

Figure 2.2. Representative scheme for amplification strategies for *Fth* and V5 identification. A) Screening of *Fth* allele in a wild type mouse using *Fth* Forward and *Fth* Reverse primers. The amplicon is expected to have 233 base pairs (bp). B) Screening of a modified Fth allele with a V5 tag sequence of 42 bp in the N-terminus. Accordingly, the amplified segment is expected to have 275 base pairs. C) Screening of a modified *Fth* allele with a V5 tag using V5 Forward and *Fth* Reverse primers. The amplicon produced in this screening should have 167 bp.

2.3.4. Polyacrylamide Gel Electrophoresis (PAGE)

After regular PCR protocol (described in 2.3.2) a PAGE gel was prepared using the following components (for 15 mL of total volume):

- Ultrapure water – 5,85 mL
- 30% Polyacrylamide (BIO-RAD Ref: 161-0156) – 7,5 mL
- Tris-Borate-EDTA (TBE buffer) 1x (220 mM Tris, 180 mM boric acid, and 5 mM EDTA)
- 10% Ammonium Persulfate (APS) (BIO-RAD Ref: 1610700) – 0,15 mL
- Tetramethylethylenediamine (TEMED) (Sigma-Aldrich Ref:T9281) – 0,009 mL

After addition of APS and TEMED, which start the polymerization process, the mixed solution was quickly added to 0.75 mm Spacer Plates for WB (BIO-RAD Ref: 1654111) and 10 well combs (BIO-RAD Ref: 1653308) were carefully placed. The gel was allowed 30 min to polymerize. After polymerization the comb was removed and the gel setup was then placed in the electrophoresis unit (BIO-RAD). 1x TBE buffer was used to fill the inner chamber, some volume was also added to the outer chamber. PCR products were added to each well alongside a Gene Ruler 100bp DNA Ladder (Thermo Scientific Ref: SM0241) and the gel ran for 3 h at 150V.

After electrophoresis, the separating gel was removed from its encasing cassette and placed in 25 mL TBE buffer with 25 µL of RedSafe Nucleic Acid Staining Solution (INTRON Ref: 21141) for 1 h. After

incubation the gel was carefully removed and the results were analyzed by UV radiation in a Gel Doc EZ Imager (BIO-RAD Ref: 170-8270).

2.4. Western Blot

2.4.1. Protein extraction from tissues

Mice were sacrificed by CO_2 narcosis until complete heart arrest. After death, mice were perfused by intracardiac injection with 20 mL of cold PBS to remove the blood out of the vasculature. Organs were collected in 1.5 mL Eppendorf tubes and snap frozen in liquid nitrogen. From this point samples can be stored at -80ºC to avoid protein degradation. Proteins were extracted from tissues by mechanic disruption of tissues in RIPA buffer (50 mM Tris-HCl ph=7.5; 150 mM NaCl; 1 mM EGTA; 1 mM Sodium Orthovanadate; 1 mM Sodium Fluoride; 1% NP40) containing a complete, EDTA Free Protease Inhibitor tablet (Roche Ref: 11 873 580 001) using a 2 mL Dounce Tissue Grinder Set (Sigma-Aldrich Ref: D8938). The mixture was then transferred into new 1.5 mL Eppendorf tubes and incubated for 20 min on ice. Disrupted tissues were then sonicated for 20 secs at 300W in the Ultrasonic Processor XL 2020 Sonicator (Misonix, Inc). The sonicated samples were spin down at 13700 g at 4ºC (Eppendorf Centrifuge 5417R). Finally, supernatants, containing proteins, were transferred to fresh Eppendorf tubes and stored at -20ºC for further quantification and western blot analysis.

2.4.2. Protein Quantification by the Bradford Assay

To quantify the amount of proteins obtained after tissue disruption we used the Bradford assay (Bradford, 1976). The Bradford reagent (BIO-RAD Ref: 500-0006) was first diluted in ultrapure water according to manufacturer guidelines. Due to high protein concentrations our protein mixture was diluted in RIPA buffer and 1 µL of the mixture was added to 1 mL of the Bradford solution and incubated at room temperature during 20-30 min in the dark. Serial dilutions of Purified Bovine Serum Albumin (New England Biolabs Ref: B9001S) were also prepared and used as our standard and 1 µL of each dilution was added to the Bradford solution and incubated for 20-30 min in the dark. Sample Absorbance was detected by spectrophotometry, measuring the wavelengths at 595 nanometers (nm) in a SmartSpec™ 3000 Spectrophotometer (BIO-RAD). RIPA buffer diluted in the Bradford solution was used as blank to zero the spectrophotometer. To create a standard curve, we plotted the 595 nm values of BSA (y-axis) versus their concentration in µg/ml (x-axis). We used the standard curve and multiplied by the dilution factor to determine the protein concentration of our samples.

2.4.3. Protein electrophoresis

Protein extracts were equally adjusted to 80 µg per sample in Laemmli Sample Buffer (BIO-RAD Ref: 161-0737) and denatured for 15-20 min at 70ºC. Given the small molecular weight of the proteins analyzed (between 21 kDa to 42 kDa) by western blot, 12% polyacrylamide gels were chosen which

allow for optimal separation in a range between 10-100 kDa. The reagents used for both Separating and Stacking gels are shown below:

Separating gel (for 10 mL total volume):

- Ultrapure water – 3.3 mL
- 30% Polyacrylamide (BIO-RAD Ref: 161-0156) – 4 mL
- 1M Tris (pH=6,8) – 2,5 mL
- 10% Sodium n-Dodecyl Sulfate (SDS) (MerckMillipore Ref: 428018) – 0,1 mL
- 10% Ammonium Persulfate (APS) (BIO-RAD Ref: 1610700) – 0,1 mL
- Tetramethylethylenediamine (TEMED) (Sigma-Aldrich Ref:T9281) – 0,004 mL

After addition of APS and TEMED, which start the polymerization process, the mixed solution was quickly added to 0.75 mm Spacer Plates for WB (BIO-RAD Ref: 1654111) or 1.5 mm Spacer Plates for WB (BIO-RAD Ref: 1653312) according to the number of samples and left to polymerize at room temperature for 1 h. After polymerization the process was repeated for the Stacking gel (for 3mL total volume):

- Ultrapure water – 2,1 mL
- 30% Polyacrylamide (BIO-RAD Ref: 161-0156) – 0,5 mL
- 1M Tris (pH=6,8) – 0,38 mL
- 10% Sodium n-Dodecyl Sulfate (SDS) (MerckMillipore Ref: 428018) – 0,03 mL
- 10% Ammonium Persulfate (APS) (BIO-RAD Ref: 1610700) – 0,03 mL
- Tetramethylethylenediamine (TEMED) (Sigma-Aldrich Ref: T9281) – 0,002 mL

APS and TEMED were combined with the other reagents and the mixed solution was added on top of the polymerized Separating gel. 10 well combs (BIO-RAD Ref: 1653308) or 15 well combs (BIO-RAD Ref: 1653365) were carefully placed before polymerization according to the number of samples. After polymerization the comb was removed and the gel setup was then placed in the electrophoresis unit (BIO-RAD). 1x Running buffer solution was prepared from 10x Running buffer (248 mM Tris(hydroxymethyl)aminomethane; 1,92 mM Glycine; 1% SDS and 1L ultrapure water) and used to fill the inner chamber, some volume was also added to the outer chamber. Samples were loaded alongside NZYColour Protein Marker II (NZY Tech Ref: MB09002) and the gel ran for 30 min at 50V or until the proteins reach the beginning of the Separating gel. From this point, the voltage was increased to 100V and the gel ran for an additional 60 min.

2.4.4. Immunobloting

After protein electrophoresis, the separating gel was removed from its encasing cassette and placed in a Transfer buffer (48 mM Tris; 39 mM Glycine; 0,5% SDS; 1L ultrapure water). A polyvinyldifluoridine membrane (PVDF) (BIO-RAD Ref: 162-0177) was cut with the same area as the gel, activated with 100% methanol for 1 min, washed with ultrapure water and placed in Transfer buffer for 5 min. The

blot was setup accordingly to the scheme presented in figure 2.3 using Extra-Thick Paper Filters (BIO-RAD Ref: 1703966). Proteins were transferred onto the PVDF by semi-dry transfer electroblotting performed using a Trans-Blot® SD Semi-Dry Electrophoretic Transfer Cell (BIO-RAD Ref: 170-3940) such as the one depicted in figure 2.3. The transfer ran for 20 min at 12V. After transfer, the membrane was blocked for 60 min in blocking buffer (5% Non-Fat Dry Milk powder in PBS; 0,1% TWEEN-20) and incubated overnight at 4ºC on a rocking platform with primary Abs (see Abs for western blot). The next day, the membrane was then washed three times with Tris-Buffered Saline Tween-20 (TBST) (pH= 7,5; 20 mM Tris; 150 mM NaCl; 0,1% Tween-20) for 15 min and incubated with secondary Abs conjugated with Horseradish Peroxidase (HRP) for 60 min at room temperature (see 2.3.5 Abs for western blot). After a repetition of the washing step for 15 min the membrane was ready for detection of the chemiluminescent substrate.

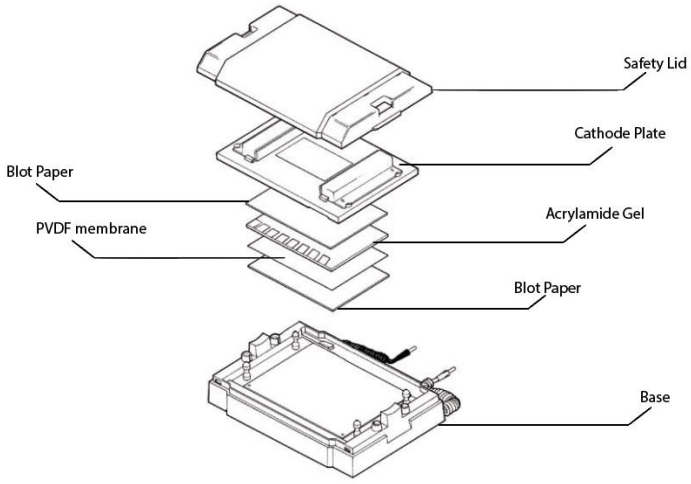

Figure 2.3. Schematic representation of the stack setup for transfer of proteins from the acrylamide gel to the PVDF membrane using a Trans-Blot® SD Semi-Dry Electrophoretic Transfer Cell. Electrical current flows from the negatively charged cathode plate to the positively charged base allowing for a continuous and homogenous current to travel along the gel to the PVDF membrane.

Detection was achieved by Pierce ECL Western Blotting Substrate (ThermoFisher Ref: 32209) or SuperSignal West Pico Chemiluminescent Substrate (ThermoFisher Ref: 34080) according to signal intensity. In our experiments, we used the same membrane to stain for FTH, V5, B-Actin and GAPDH. FTH and V5 proteins have very similar molecular weights (differing in approximately 1.5 kDa). To accurately distinguish between stainings and to remove previous background staining or non-specific binding, subsequent membrane stripping was needed. Membranes were incubated two times with Stripping Buffer (200 mM Glycine; 3,5 mM SDS; 1% Tween-20 in 1L ultrapure water) for 10 min each at room temperature and extensively washed in PBS (two times, 10 min at room temperature under soft agitation). Subsequent washings with TBST were also performed (two times, 5 min at room temperature under soft agitation). Thereafter the membrane was blocked with 5% non-fat dry milk powder in TBST for 1h at room temperature ready to use for protein staining.

2.4.5. Abs for western blot

Incubation with primary Abs occurred overnight at 4ºC with primary Abs directed against Ferritin Heavy Chain, V5 epitope, B-Actin and GAPDH. Peroxidase conjugated secondary Abs were used for signal detection. Full list of Ab specifications is presented in Table 2.4.

Table 2.4. Abs used for western blot experiments with the isotype, dilution, source and reference.

Ab	Isotype	Dilution	Source	Reference
Anti-FTH (monoclonal)	Rabbit IgG	1:1000	Cell Signaling	4393
Anti-V5 (monoclonal)	Mouse IgG2a	1:5000	Invitrogen	R96025
Anti-V5 (polyclonal)	Goat N/A	1:5000	Abcam	AB9137
Anti-GAPDH (polyclonal)	Goat N/A	1:5000	SICGEN	AB0049-200
Anti-b-actin (monoclonal)	Mouse IgG1	1:1000	Sigma-Aldrich	A5441
HRP conjugated anti-rabbit (polyclonal)	Goat IgG	1:5000	SantaCruz Biotechnology	sc-2030
HRP conjugated anti-mouse (polyclonal)	Goat IgG	1:5000	SantaCruz Biotechnology	sc-2005
HRP conjugated anti-goat (polyclonal)	Donkey IgG	1:5000	ThermoFisher Scientific	PA1-28664

2.5. Immunohistochemistry

2.5.1. Immunostaining in paraffin sections

Mice were sacrificed by CO_2 narcosis until a complete heart arrest was reached. After death, mice were perfused by intracardiac injection with 20mL of PBS to remove the blood out of the vasculature. The organs were collected and stored in 10% formalin, embedded in paraffin and cut into 3μm cross sections by the IGC histopathology department. After deparaffinization slides were placed in Sodium Citrate Buffer (10 mM Sodium Citrate, 0.05% Tween 20, 1 L ultrapure water, pH=6.0) and heated for 2 min at 750W in the microwave, and 4 min at 150W. The slides were then left to cool at room temperature and permeabilized with 0, 3% Triton/PBS for 15 min. Slides were blocked with commercial Goat serum

(Rockland Ref: D104-00-0050) for 60 min at room temperature and incubated with primary Abs (see 3.4.2 Abs for immunofluorescence) overnight at 4ºC in a dark wet chamber. After 3 times washing with TBST (5 min each), tissue sections were incubated with fluorophore labeled secondary Abs (see 2.5.2 Abs for immunofluorescence in paraffin sections) for 2 h at room temperature in a dark wet chamber. Afterwards, slides were washed with TBST again and then with PBS for 10 min and mounted with Mowiol Mounting Medium (Sigma-Aldrich Ref: M1289-10ML) with 10 μg /mL of 4',6-diamidino-2-phenylindole (DAPI). Mounted slides can be directly utilized for microscopy or stored in the dark at -20ºC to avoid photobleaching and allow for optimal fluorophore preservation. Images were acquired by fluorescence microscopy (see 2.6 imaging).

2.5.2. Abs for immunofluorescence in paraffin sections

For the immunofluorescence protocol in paraffin sections, detection of FTH, V5 and F4/80 was achieved with rabbit mAb directed against FTH, mouse mAb directed against V5 and rat mAb directed against F4/80. Slides were quickly washed and incubated with secondary Abs Alexa 647 Goat anti-Rabbit, Alexa 568 Goat anti-Mouse and Alexa 647 Goat anti-Rat for FTH, V5 and F4/80 detection respectively. Full list of Ab specifications is presented in Table 2.5.

Table 2.5. Abs used for immunofluorescence in paraffin sections with the isotype, source and references.

Ab	Isotype	Dilution	Source	Reference
Anti-FTH (monoclonal)	Rabbit IgG	1:100	Cell Signalling	4393
Anti-V5 (monoclonal)	Mouse IgG	1:100	Invitrogen	R96025
Anti-F4/80 (monoclonal)	Rat IgG2a, κ	1:100	BioLegend	123102
Alexa 647 conjugated anti-rabbit (polyclonal)	Goat IgG	1:500	ThermoFisher	A-10523
Alexa 568 conjugated anti-mouse (polyclonal)	Goat IgG	1:500	ThermoFisher	A-11031
Alexa 568 conjugated anti-rat (polyclonal)	Goat IgG	1:500	ThermoFisher	A-11077

2.5.3. Immunostaining in Whole-mount sections

Immediately after sacrifice, an intracardiac injection of 20 mL of PBS was administered to perfuse the blood out of the vasculature. Subsequently, an additional intracardiac injection of 10 mL of 4% paraformaldehyde (PFA) prepared from a stock solution of 16% PFA (Alfa Aesar Ref: 043368-9M) was administered for fixation of the tissues and vasculature. Furthermore, the organs were excised and placed in a 4% PFA solution in a rolling platform overnight. Following the fixation, the organs were left to wash overnight with PBS at 4ºC. After washing the organs were fixed in a 12 well plate with 4% low-melting point agarose solution (Invitrogen Ref: 15517-014) for 2 h. 100 μm sections were obtained with a Leica Vibratome VT 1000 S (Leica Biosystems) and placed in small eppendorfs with PBDO permeabilization solution (1% Bovine Serum Albumin; 1% DMSO; 0.6 % Triton X-100 in PBS) overnight at 4ºC. Afterwards, organs slices were incubated with primary Abs overnight at 4ºC (see 2.4.3 Abs for immunofluorescence). The removal of non-binding Abs was achieved through further overnight washing with PBDO permeabilization solution at 4ºC. Tissues were then incubated with Cy5 fluorophore conjugated donkey anti-goat secondary IgG overnight at 4ºC (see 2.4.4 Abs for immunostaining in Whole-mount sections). After additional washing with PBDO overnight at 4ºC, incubation with the remaining secondary Abs (see 2.5.4 Abs for immunostaining) was done overnight at 4ºC. Finally, following another day of washing with PBDO the slices were mounted with Mowiol mounting medium with 10 μg/mL of DAPI. Mounted slides can be directly observed in the microscope or stored in the dark at -20ºC. Images were acquired by confocal microscopy (see 2.6 Imaging).

2.5.4. Abs for immunostaining in Whole-mount sections

For the immunofluorescence protocol in whole-mount sections, detection of FTH, V5, F4/80 and CD68 was achieved with rabbit mAb directed against FTH, goat polyclonal Ab against V5, rat mAb against F4/80 and rat mAb against CD68. Slides were quickly washed and to avoid binding to the remaining secondary Abs the fluorophore-conjugated secondary Ab Donkey anti-Goat Alexa 647 for V5 detection was incubated first. After washing, the remaining secondary Abs Alexa 568 Goat anti-Rabbit and Alexa 568 Goat anti-Rat for FTH, F4/80 and CD68 detection respectively. Full list of Ab specifications is presented in Table 2.6.

Table 2.6. Abs used for immunofluorescence in whole-mount sections with the isotype, source and references.

Ab	Isotype	Dilution	Source	Reference
Anti-FTH (monoclonal)	Rabbit IgG	1:100	Cell Signalling	4393
Anti-V5 (polyclonal)	Goat N/A	1:200	Abcam	AB9137
Anti-F4/80 (monoclonal)	Rat IgG2a, κ	1:50	BioLegend	123102
Anti-CD68 (monoclonal)	Rat IgG2a	1:200	BIO-RAD	MCA1957
Cy5 conjugated anti-goat (polyclonal)	Donkey IgG	1:500	Jackson IR	705-175-147
Alexa 568 conjugated anti-rabbit (polyclonal)	Goat IgG	1:500	ThermoFisher	A-11011
Alexa 568 conjugated anti-rat (polyclonal)	Goat IgG	1:500	ThermoFisher	A-11077

2.6. Imaging

The two different immunohistochemistry protocols used involved different types of microscopy and by extension, two different microscopes:

- Paraffin sections were visualized by fluorescence microscopy using a commercial Leica High Content Screening microscope based on Leica DMI6000 equipped with a Hamamatsu Flash 4.0 LT sCMOS camera, using a 20x non-oil immersion objective and 40x oil immersion objective. DAPI + GFP and filtersets were controlled with the Leica LAS X software.
- Images from whole-mount sections were acquired on a commercial Leica SP5 confocal based on Leica DM6000 inverted microscope equipped with an Argon-ion laser (458, 476, 488, 514 nm lines) + 561 nm and 633 nm lasers. DAPI + GFP and filtersets were controlled with the Leica LAS X software.

2.7. Statistical Analysis

Statistical analysis was performed in GraphPad Prism v6. Nonparametric Mann-Whitney *U* test was used to assess statistical significance between two groups. Mean differences between groups were analyzed using One-way ANOVA test. Log-rank test was used when survival was assessed as an end-point. P-values significances for each statistical test performed are presented in the figure legends.

3. Results

3.1. FTH is required to maintain homeostasis and sustain survival in adulthood.

FTH protects cells from oxidative agents such as Fe^{2+}, O_2 and H_2O_2 (Theil, 2013). Under pathological conditions, disruption of systemic Fe homeostasis is associated with alterations of *Fth* expression that may contribute to the progression of certain diseases (Arosio et al., 2017; Papanikolaou and Pantopoulos, 2017), such as Parkinson, Alzheimer, atherosclerosis, pulmonary inflammatory states and rheumatoid arthritis (Torti and Torti, 2002). This is also the case for immune mediated inflammatory diseases in which FTH appears to regulate inflammation and immunity to infection as well as metainflammation (Torti and Torti, 2002; Nairz et al., 2016; Weis et al., 2017). Conditional deletion of the *Fth* allele in mice promotes tissue damage (Darshan et al., 2009) and inflammation (Bolisetty et al., 2015) and is essential to support homeostasis in response to systemic infections (Gozzelino et al., 2012; Weis et al., 2017). Given the embryonic lethality of *Fth* knockout mice (Ferreira et al., 2000) a new system was needed to assess the role of FTH in a fully developed organism. Therefore, we made use of ROSA26$^{Cre\text{-}ERT2}$ mice, which express the Cre recombinase fused to a modified Tamoxifen responsive estrogen receptor under the ubiquitous and strong promoter ROSA26 (henceforth referred to as *R26*). The *R26* mice were crossed with *Fth*$^{lox/lox}$ mice to generate *R26.Fth*$^{lox/lox}$ mice where the *Fth* allele is flanked by two loxP sites (Figure 3.1A). Upon Tamoxifen administration, activation of the Cre recombinase excises the region of *Fth* allele flanked by the loxP sites, thus generating mutant alleles that suppress *Fth* expression (*R26.Fth*$^{\Delta/\Delta}$) (Figure 3.1B).

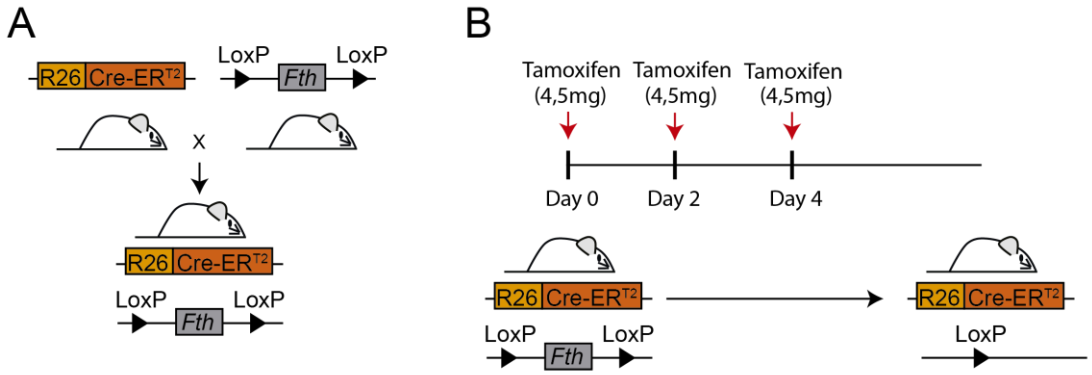

Figure 3.1. Deletion of *Fth* by Tamoxifen administration. A) Schematic representation of the generation of Rosa26$^{CreER\text{-}T2}$*Fth*$^{lox/lox}$ mice showing Cre fused with the Tamoxifen responsive estrogen receptor 2 (ER-T2) under control of the ubiquitously expressed Rosa26 (*R26*) promoter. The ferritin heavy chain (FTH) gene is flanked by LoxP sites represented as black triangles. Scheme depicting Tamoxifen administration for the deletion of *Fth* in this mouse model showing excision of the *Fth* allele and one LoxP site after Tamoxifen-induced Cre activation. Red arrows represent the time of Tamoxifen administration (4.5mg of Tamoxifen/mouse). Tamoxifen was administered by oral gavage 3 times in the course of one week.

Deletion of the *Fth* allele was performed in 8 week-old mice and assessed by real time PCR on several tissues showing complete deletion in all tissues analyzed (Figure 3.2A) except the heart that showed some residual *Fth* mRNA expression and more evidently in the brain, where approximately 30% of *Fth* mRNA expression was retained (Figure 3.2A). We also confirmed the FTH deletion at the protein level, by western blot (Figure 3.2B-E). Expression of *Fth* in the heart was reduced by 60 to 75% (Figure 3.2C) in *R26.Fth*$^{\Delta/\Delta}$ mice, as compared to control *Fth*$^{lox/lox}$ mice receiving Tamoxifen. In the kidneys there was a general reduction of FTH protein level in *R26.Fth*$^{\Delta/\Delta}$ vs. *Fth*$^{lox/lox}$ mice, although this was not significant due to the high variation observed between samples from *Fth*-deleted mice (Figure 3.2D). Of the four *R26.Fth* $^{\Delta/\Delta}$ mice used for *Fth* deletion, three were efficiently deleted, whereas one still displayed considerable *Fth* expression, comparable to control *Fth*$^{lox/lox}$ mice (Figure 3.2D). In contrast, *Fth* protein expression was virtually absent in the liver (Figure 3.2B) and lungs (Figure 3.2E) of *R26.Fth*$^{\Delta/\Delta}$ vs. *Fth*$^{lox/lox}$ mice. Of note *Fth* expression in both organs displayed high variability at steady-state (Figure 3.2B, E).

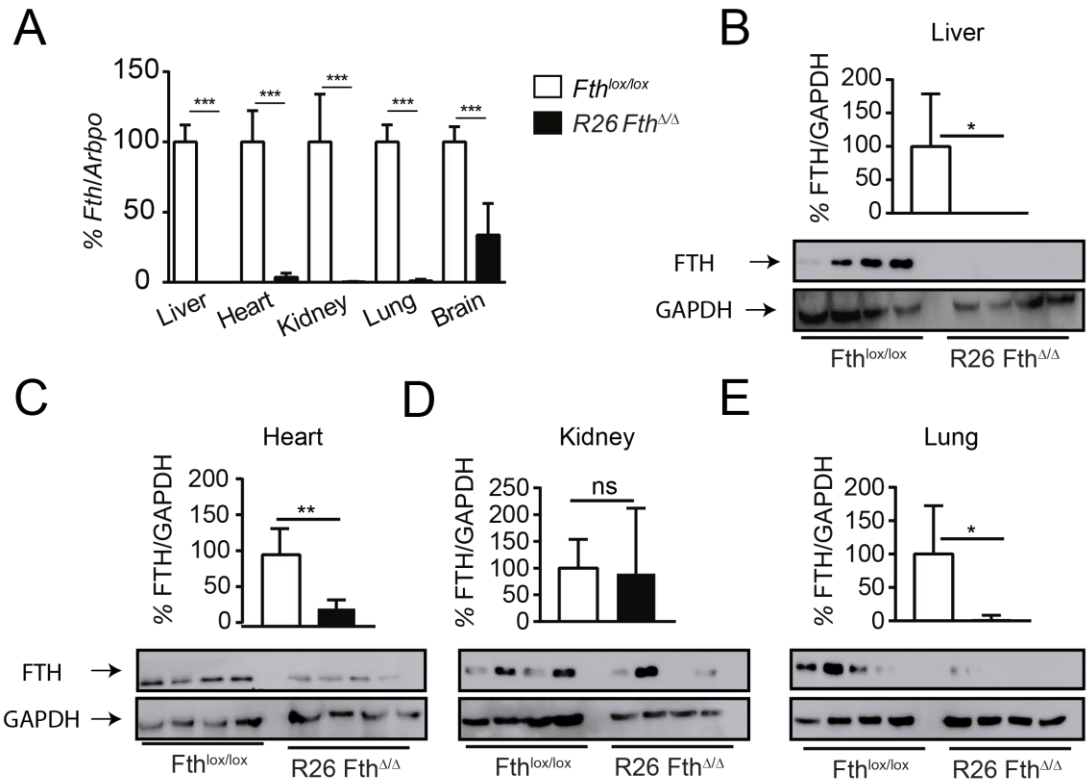

Figure 3.2. *Fth* mRNA and protein levels after Tamoxifen induced deletion. A) Representative real time PCR confirming deletion of the *Fth* gene after Tamoxifen administration in the liver, heart, kidney, lungs and brain of *R26.Fth*$^{\Delta/\Delta}$ (n=6) and control *Fth*$^{lox/lox}$ mice (n=4), courtesy of Birte Blankenhaus. B-E) FTH western blot from *Fth*$^{lox/lox}$ (n=4) and *R26.Fth*$^{\Delta/\Delta}$ (n=4) mice showing a general decrease in FTH protein levels after Tamoxifen deletion. Relative expression was normalized to Gapdh control in the liver (B), heart (C), kidney (D) and lung (E). *P<0,05, **P<0,005.

Having confirmed the ability to delete *Fth* both at the mRNA and the protein levels, characterization of these mice was pursued considering their ability to maintain a homeostatic

range on several parameters such as body weight and temperature. One week after *Fth* deletion, *R26.Fth*$^{\Delta/\Delta}$ animals exhibited a dramatic decrease in body weight (Figure 3.3A) and temperature (Figure 3.3B), ultimately leading to death within 16 days (Figure 3.3C). This demonstrates that *Fth* expression is essential for maintenance of homeostasis in adult mice.

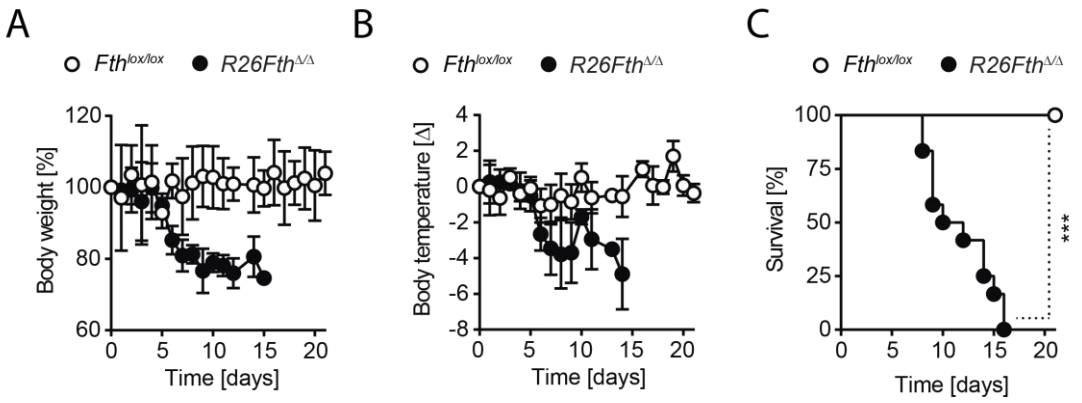

Figure 3.3. FTH is required to sustain survival in adulthood. Body weight (A), body temperature (B) and survival (C) curves of *Fth*$^{lox/lox}$ (n=7) and *R26.Fth*$^{\Delta/\Delta}$ (n=12) mice after deletion by Tamoxifen showing sharp decreases in weight and temperature and ultimately death of *R26.Fth*$^{\Delta/\Delta}$ mice after *Fth* deletion. Courtesy of Birte Blankenhaus. *P<0,05, **P<0,005, ***P<0,001.

3.2. Macrophage-derived FTH is sufficient to maintain homeostasis.

Previous studies using tissue-specific Cre recombinase-mediated deletion of the *Fth*$^{lox/lox}$ did not show impairment of survival (Darshan et al., 2009; Vanoaica et al., 2010; Gozzelino et al., 2012; Bolisetty et al., 2015, 2016; Weis et al., 2017). This suggested the existence of some unknown homeostatic compensatory mechanisms that may counteract the lack of *Fth* in parenchyma tissues. Interestingly, macrophages have been shown to play important roles in the maintenance of homeostasis in situations where Fe imbalances occur (Ward et al., 2011; Theurl et al., 2016; Nairz et al., 2017). In keeping with this notion, bone marrow-derived macrophages expressing the heme catabolizing enzyme HO-1 have been shown to prevent heme-related cytotoxicity when expression of HO-1 is absent in parenchyma tissues (Kovtunovych et al., 2014). We took advantage of our model to interrogate the functional contribution of hematopoietic versus non-hematopoietic compartment in the maintenance of homeostasis and survival following *Fth* deletion. Given the capacity of hematopoietic cells to fully regenerate all circulating cells and repopulate tissues in a myeloablated recipient (McGrath et al., 2015), *R26*$^{CreER\text{-}T2}$.*Fth*$^{lox/lox}$ and control *Fth*$^{lox/lox}$ mice were lethally irradiated and reconstituted with bone marrow from *R26*$^{CreER\text{-}T2}$.*Fth*$^{lox/lox}$ or *Fth*$^{lox/lox}$ mice (Figure 3.4A). As expected, control *Fth*$^{lox/lox}$ recipients reconstituted with *Fth*$^{lox/lox}$ bone marrow survived subsequent Tamoxifen administration, not associated with *Fth* deletion, i.e. *Fth*$^{lox/lox}$→*Fth*$^{lox/lox}$ mice (Figure 3.4B). In contrast, *R26*$^{CreER\text{-}T2}$*Fth*$^{lox/lox}$ recipients

reconstituted with *R26*$^{\text{CreER-T2}}$*Fth*$^{lox/lox}$ bone marrow lost body weight and temperature (Figure 3.4C and D), succumbing within 20 days after Tamoxifen-induced deletion of the *Fth*$^{lox/lox}$ allele, *R26.Fth*$^{\Delta/\Delta}$→ *R26.Fth*$^{\Delta/\Delta}$ mice (Figure 3.4B). Surprisingly, *Fth*$^{lox/lox}$ recipients reconstituted with *Fth*$^{lox/lox}$ bone marrow did not succumb to Tamoxifen-induced deletion of the *Fth*$^{lox/lox}$ allele in parenchyma tissues, i.e. *Fth*$^{lox/lox}$ →*R26.Fth*$^{\Delta/\Delta}$ mice (Figure 3.4B).

Taking into account the role of macrophages and myeloid-derived cells in Fe homeostasis (Soares and Hamza, 2016), we hypothesized that the capacity of bone marrow derived cells to supplement for *Fth* deletion in parenchyma tissues was likely mediated by the expression of FTH in bone marrow-derived monocyte/macrophages. To test this hypothesis, we generated *LysM*$^{\text{Cre}}$*Fth*$^{\Delta/\Delta}$ animals (Figure 3.4A) where expression of Cre recombinase under the control of the *LysM* promotor, driving Cre expression specifically in the myeloid lineage, more specifically in macrophages (Clausen B.E et al., 2001). Since this promoter is constitutively expressed, macrophages lack *Fth* expression from birth. Lethal-irradiated *R26.Fth*$^{lox/lox}$ recipients reconstituted with *LysM*$^{\text{Cre}}$*Fth*$^{\Delta/\Delta}$ bone marrow loss body weight and temperature, succumbing within 40 days of Tamoxifen-induced deletion of the *Fth*$^{lox/lox}$ allele in parenchyma tissues (Figure 3.4C, D), with the remaining animals eventually succumbing after 80 days, i.e. *LysM*$^{\text{Cre}}$*Fth*$^{\Delta/\Delta}$ →*R26.Fth*$^{\Delta/\Delta}$ mice (Figure 3.4B).

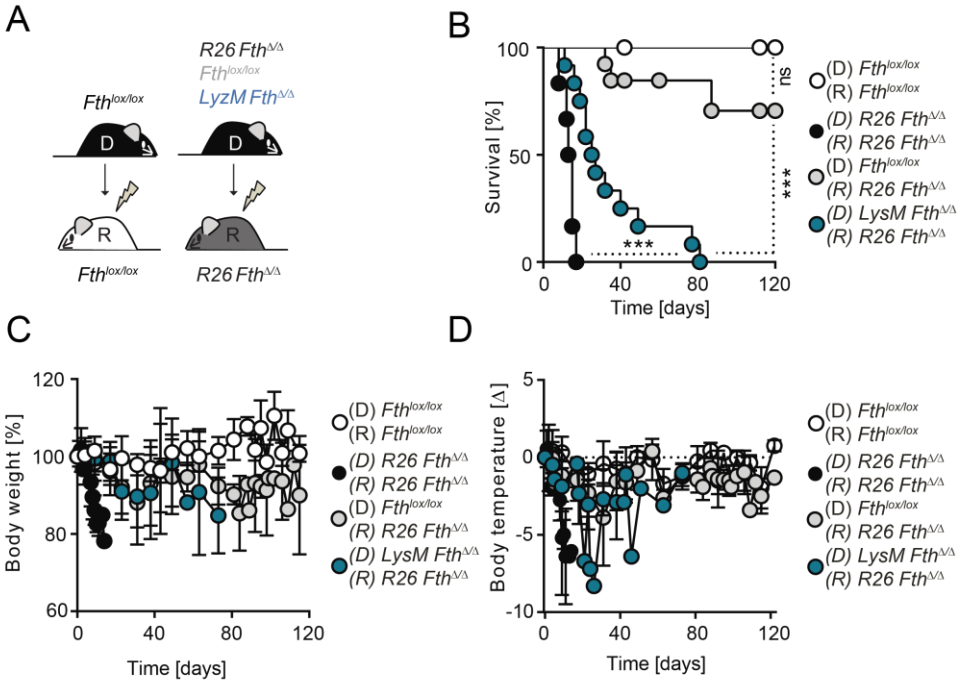

Figure 3.4. Influence of *Fth* expression by hematopoietic cells in chimeric mice. A) Schematic representation of bone marrow chimeras generated by irradiation of *Fth*$^{\text{lox/lox}}$ and *R26*$^{\text{CreER-T2}}$*Fth*$^{\text{lox/lox}}$ mice. "D" represents the bone marrow donor mice and "R" represents the bone marrow receptor mice after the irradiation. B) Survival of *Fth*$^{\text{lox/lox}}$→*Fth*$^{\text{lox/lox}}$ (n=7), *R26*$^{\text{CreER-T2}}$*Fth*$^{\Delta/\Delta}$→*R26*$^{\text{CreER-T2}}$*Fth*$^{\Delta/\Delta}$ (n=6), *Fth*$^{\text{lox/lox}}$→*R26*$^{\text{CreER-T2}}$*Fth*$^{\Delta/\Delta}$ (n=10), and *LysM*$^{\text{Cre}}$*Fth*$^{\Delta/\Delta}$→*R26*$^{\text{CreER-T2}}$*Fth*$^{\Delta/\Delta}$ (n=9). Body weight and temperature are presented in C) and D) respectively. Courtesy of Birte Blankenhaus. *P<0,05, **P<0,005, ***P<0,001.

Next, we asked to what extent monocytes/macrophages complement the lack of FTH in this context. For this purpose we isolated heart, kidney, lungs and liver from *Fth*$^{lox/lox}$→*Fth*$^{lox/lox}$, *Fth*$^{lox/lox}$→*R26.Fth*$^{\Delta/\Delta}$ and *LysM*^{Cre}*Fth*$^{\Delta/\Delta}$→*R26.Fth*$^{\Delta/\Delta}$ chimeras and assessed the levels of FTH by western blot. *Fth*$^{lox/lox}$→*Fth*$^{lox/lox}$ mice exhibited normal levels of FTH expression in heart, kidney, lungs and liver (Figure 3.5A-D). Although *Fth*$^{lox/lox}$→*R26.Fth*$^{\Delta/\Delta}$ mice also express FTH in these organs (Figure 3.5A-D), the levels of FTH expression were decreased (Figure 3.5A-D), as compared to control *Fth*$^{lox/lox}$→*Fth*$^{lox/lox}$ mice (Figure 3.5A-D). In contrast, FTH protein levels were virtually absent in the liver, kidneys and lungs of *LysM*^{Cre}*Fth*$^{\Delta/\Delta}$→*R26.Fth*$^{\Delta/\Delta}$ mice, suggesting that the majority of the hematopoietic FTH is expressed by monocyte/macrophages (Figure 3.5A, C, D). However, FTH expression in the hearts of *LysM*^{Cre}*Fth*$^{\Delta/\Delta}$→*R26.Fth*$^{\Delta/\Delta}$ mice does not appear to be significantly different from FTH levels of *Fth*$^{lox/lox}$→*R26.Fth*$^{\Delta/\Delta}$ mice (Figure 3.5B). Taken together, these data demonstrate that when FTH expression is decreased in parenchyma tissues, expression of FTH by macrophages is critical to complement this deficiency, sustaining homeostasis and ultimately life.

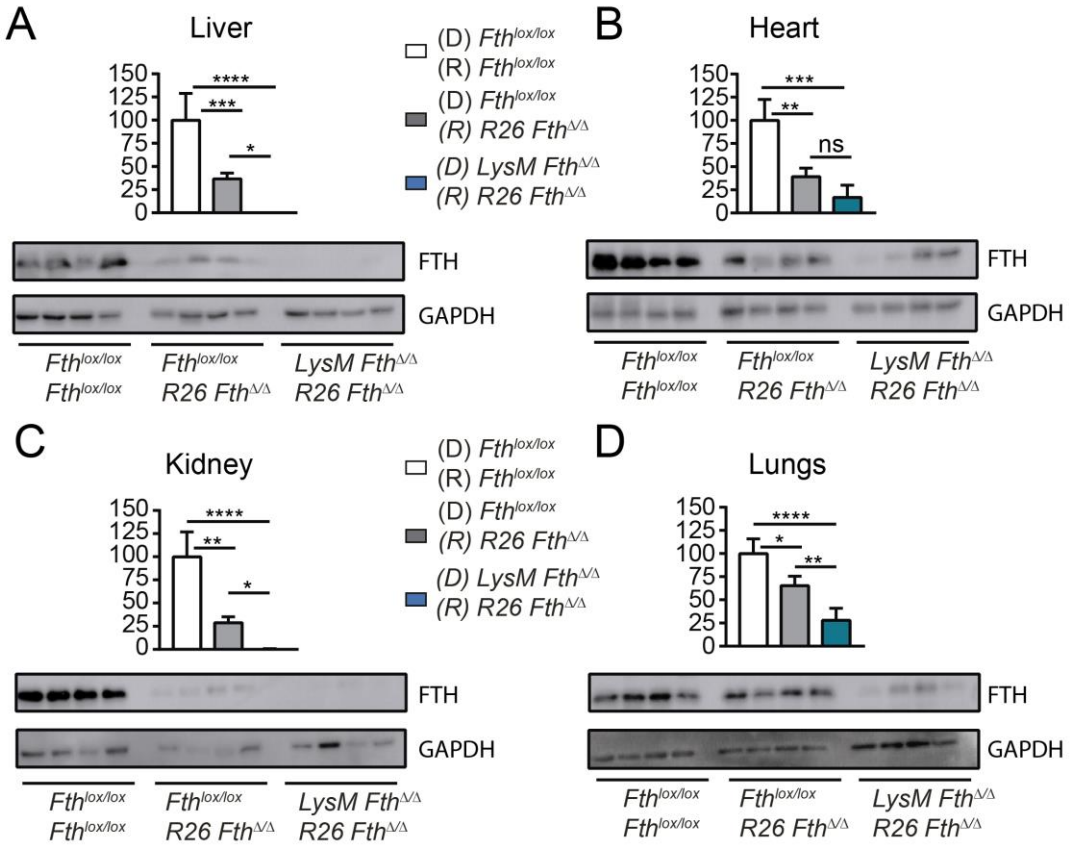

Figure 3.5. Contribution to FTH parenchyma levels by the LysM compartment. Western blot and quantification of FTH in liver (A), heart (B), kidney (C) and lungs (D) of *Fth*$^{lox/lox}$→*Fth*$^{lox/lox}$ (n=4), *Fth*$^{lox/lox}$→*R26*$^{CreER\text{-}T2}$*Fth*$^{\Delta/\Delta}$ (n=4), and *LysM*^{Cre}*Fth*$^{\Delta/\Delta}$→*R26*$^{CreER\text{-}T2}$*Fth*$^{\Delta/\Delta}$ (n=4) chimeric mice. FTH expression was normalized to GAPDH. *Fth*$^{lox/lox}$→*Fth*$^{lox/lox}$ mice represents 100% expression of FTH and the other groups were normalized to the expression of this control group. *P<0,05, **P<0,005, ***P<0,001, ****P<0,0001.

3.3. Identification of specific macrophage populations involved in the rescue of *Fth*-deleted mice.

The origin of macrophages in mammals is still a matter of debate. The actual paradigm stipulates that tissue-resident macrophages, which have specialized function in tissues arise during fetal development (Gomez Perdiguero et al., 2014) and need to express the chemokine receptor CX_3CR1 to migrate and develop in specific fetal tissues (Varol et al., 2015). At adulthood two main mechanisms occur at steady-state to maintain the pool of these cells. The first one is self-renewal and is observed mainly in the heart, brain and kidney (Varol et al., 2015). However, as the host ages or is subjected to tissue injury, circulating monocytes can transdifferentiate into functional tissue-resident macrophages (Perdiguero and Geissmann, 2015). Having established that the expression of FTH by macrophages is essential to restore survival of *R26.Fth*$^{\Delta/\Delta}$ mice (Figure 3.4B), the question arose if expression of FTH in either circulating monocytes or tissue resident macrophages was responsible for this phenomenon. We used for that purpose *Ccr2* deficient (*Ccr2*$^{-/-}$) mice in which the absence of this chemokine receptor prevents monocyte migration from the bone marrow into parenchymal tissues (Boring et al., 1997; Varol et al., 2015). We assumed that bone marrow macrophages from *Ccr2*$^{-/-}$ presumably still express normal levels of ferritin that upon secretion could possibly sustain the survival of *R26.Fth*$^{\Delta/\Delta}$ recipient mice reconstituted with *Ccr2*$^{-/-}$ bone marrow, i.e. *Ccr2*$^{-/-}$→*R26.Fth*$^{\Delta/\Delta}$ mice. Upon deletion of the *Fth* allele (Figure 3.6A), *Ccr2*$^{-/-}$→*R26.Fth*$^{\Delta/\Delta}$ mice gradually lost body weight (Figure 3.6C) and more evidently lost body temperature (Figure 3.6D), when compared to control *Fth*$^{lox/lox}$→*Fth*$^{lox/lox}$ mice. Tamoxifen-induced *Fth* deletion in *Ccr2*$^{-/-}$→*R26.Fth*$^{\Delta/\Delta}$ mice led to 80% death (Figure 3.6B). However, the kinetic of death was delayed, as compared to *LysM*^{Cre}*Fth*$^{\Delta/\Delta}$→*R26.Fth*$^{\Delta/\Delta}$ mice, what the majority of *Ccr2*$^{-/-}$→*R26.Fth*$^{\Delta/\Delta}$ mice dying approximately 100 days after *Fth* deletion.

This could be due to the presence of a monocyte subset that can still migrate into injured/stress tissues and support tissue function and life for a certain amount of time. Accordingly, a recent work showed the existence of splenic reservoir monocytes that can migrate to stressed and injured tissues independently of *Ccr2* (Swirski et al., 2009). To test this hypothesis, lethally irradiated *R26.Fth*$^{\Delta/\Delta}$ and control *Fth*$^{lox/lox}$ mice were reconstituted with wild-type bone marrow. Under the assumption that bone marrow derived cells can repopulate the spleen after irradiation, the subsequent removal of the spleen would eliminate this specific population of infiltrating monocytes and therefore wild type bone marrow would not be sufficient to rescue *R26.Fth*$^{\Delta/\Delta}$ hosts in the absence of the spleen. 8 weeks after reconstitution, we performed a splenectomy, waited for the recovery of animals and induced deletion of *R26.Fth*$^{\Delta/\Delta}$ by Tamoxifen administration. We then monitored the survival of these animals. For technical reasons the non-splenectomized control *Fth*$^{lox/lox}$→*R26.Fth*$^{\Delta/\Delta}$ mice died (Figure 3.7A), and as such, further experiments are necessary to reassess the technical conditions required for these experiments.

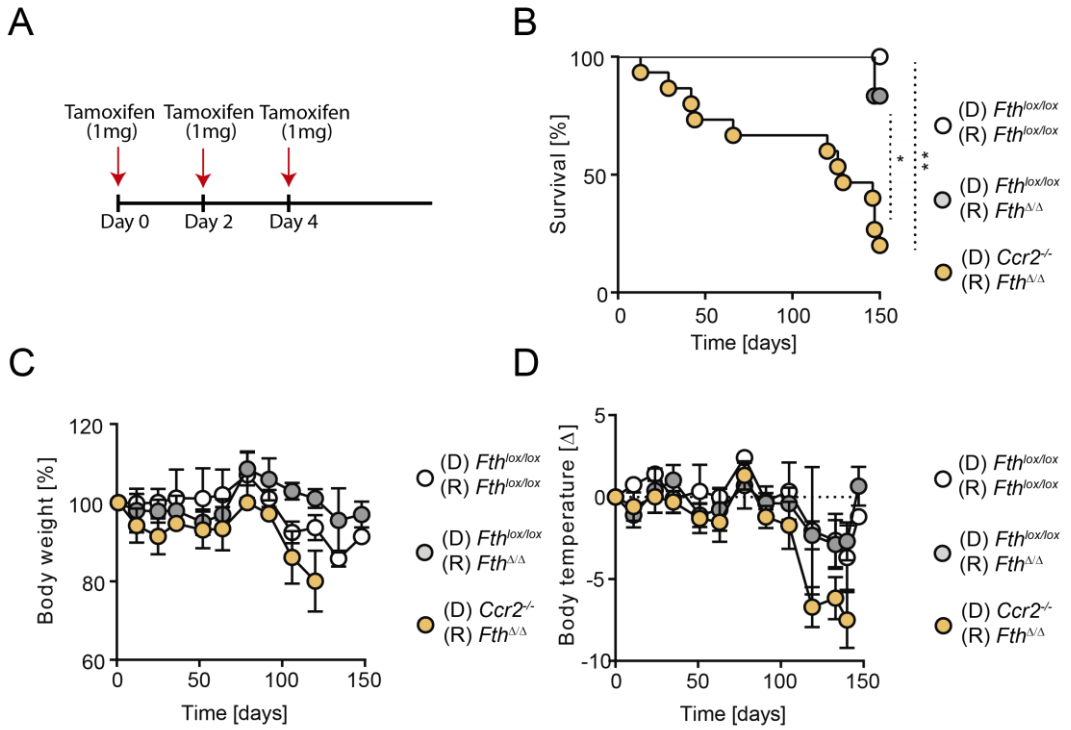

Figure 3.6. Impact of *Ccr2* expression on the survival of *Fth* deleted mice. A) Tamoxifen regime administered to these mice by oral gavage, 3 times in the course of one week. B) Survival curve after Tamoxifen induced deletion of *Fth* in *Ccr2*$^{-/-}$→*R26.Fth*$^{\Delta/\Delta}$ (n=8) and control *Fth* $^{lox/lox}$→*Fth*$^{lox/lox}$ (n=4), *Fth*$^{lox/lox}$→*R26.Fth*$^{\Delta/\Delta}$ (n=4) mice. C) Body weight and temperature (D) after deletion. Red arrows represent the time of Tamoxifen administration (1mg/mouse). *P<0,05, **P<0,005.

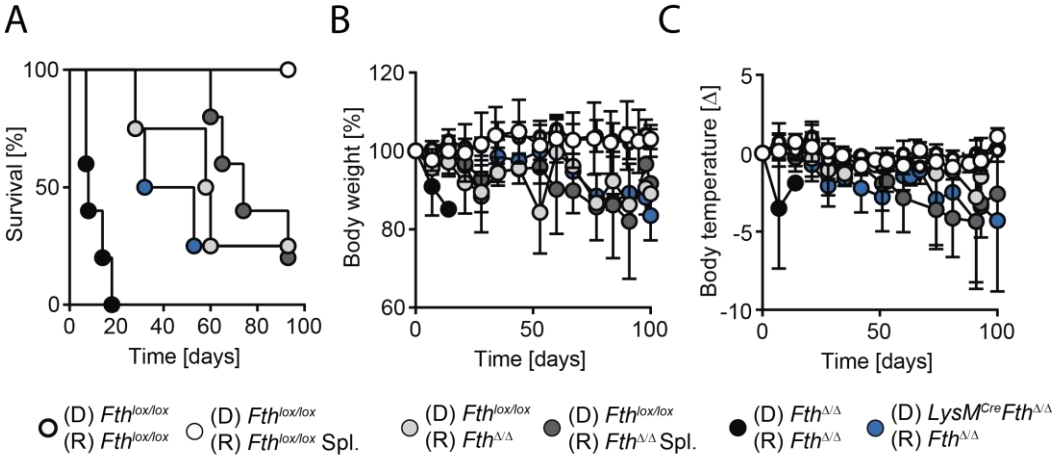

Figure 3.7. Influence of splenectomy on *Fth* deletion in bone marrow chimeric mice. A) Survival of splenectomised *Fth*$^{lox/lox}$→*Fth*$^{lox/lox}$ (n=5), *Fth*$^{lox/lox}$→*R26.Fth*$^{\Delta/\Delta}$ (n=5) and non-splenectomized control *Fth*$^{lox/lox}$→*R26.Fth*$^{\Delta/\Delta}$ (n=6), *R26.Fth*$^{\Delta/\Delta}$→*R26.Fth*$^{\Delta/\Delta}$ (n=6) and LysM^{Cre}*Fth*$^{\Delta/\Delta}$→*R26.Fth*$^{\Delta/\Delta}$ (n=9) mice upon *Fth* deletion. Body weight and temperature after *Fth* deletion are presented in (B) and (C) respectively. "Spl." indicates groups that were splenectomised before Tamoxifen administration.

As *Cx$_3$cr1* expression is required for both recruitment and retention of tissue resident macrophages (Pittet et al., 2014), being highly expressed in tissue-resident myeloid cells (Geissmann et al., 2003; Yona et al., 2013), we investigated whether *Fth* expression in CX_3CR1^+ cells rescued the survival of *R26.Fth*$^{\Delta/\Delta}$ mice. To test this hypothesis we generated chimeric mice in which *Fth* was deleted in an inducible manner in CX_3CR1^+ cells. However, due to the self-renewable characteristics of CX_3CR1^+ macrophage populations, there is a constant generation of bone marrow derived CX_3CR1^+ cells that must be continuously exposed to Tamoxifen-induced deletion, requiring an adjustment of the Tamoxifen regimen. Therefore we applied a prolonged Tamoxifen regimen in order to achieve a sustained deletion of *Fth* in the CX_3CR1^+ population. Tamoxifen was given two times a week during 3 weeks, in contrast to the original *Fth* deletion protocol which involved 3 administrations in the span of a week (Figure. 3.1B). Constant Tamoxifen treatment and concomitant *Fth* deletion proved to be exceedingly severe and led to loss of body weight (Figure 3.8B) and temperature (Figure 3.8C), and death of 50% of the *R26.Fth*$^{\Delta/\Delta}$ mice, which received wild-type bone marrow (Figure 3.8A). In order to circumvent this, we switched to Tamoxifen food, allowing for constant Tamoxifen exposure and *Fth* deletion. However, administration of Tamoxifen food also led to death of chimeric *Fth*$^{lox/lox}$→*R26.Fth*$^{\Delta/\Delta}$ mice, which does not allow to assess the significance of *Fth* deletion in chimeric *Cx$_3$cr1*$^{Cre\text{-}ERT2}$*Fth*$^{\Delta/\Delta}$→*R26.Fth*$^{\Delta/\Delta}$ mice (Figure 3.8D), which decreased body weight (Figure 3.8E) and temperature (Figure 3.8F). However, chimeric *Fth*$^{lox/lox}$→*R26.Fth*$^{\Delta/\Delta}$ mice succumbed with different kinetics from *Cx$_3$cr1*$^{Cre\text{-}ERT2}$*Fth*$^{\Delta/\Delta}$→*R26.Fth*$^{\Delta/\Delta}$ mice, with most *Fth*$^{lox/lox}$→*R26.Fth*$^{\Delta/\Delta}$ mice succumbing 50 days after Tamoxifen administration. While these technical issues prevent from drawing firm conclusions at this point, the data suggests that *Fth*-competent CX_3CR1^+ macrophages are important to sustain homeostasis when expression of *Fth* is deleted in parenchyma cells.

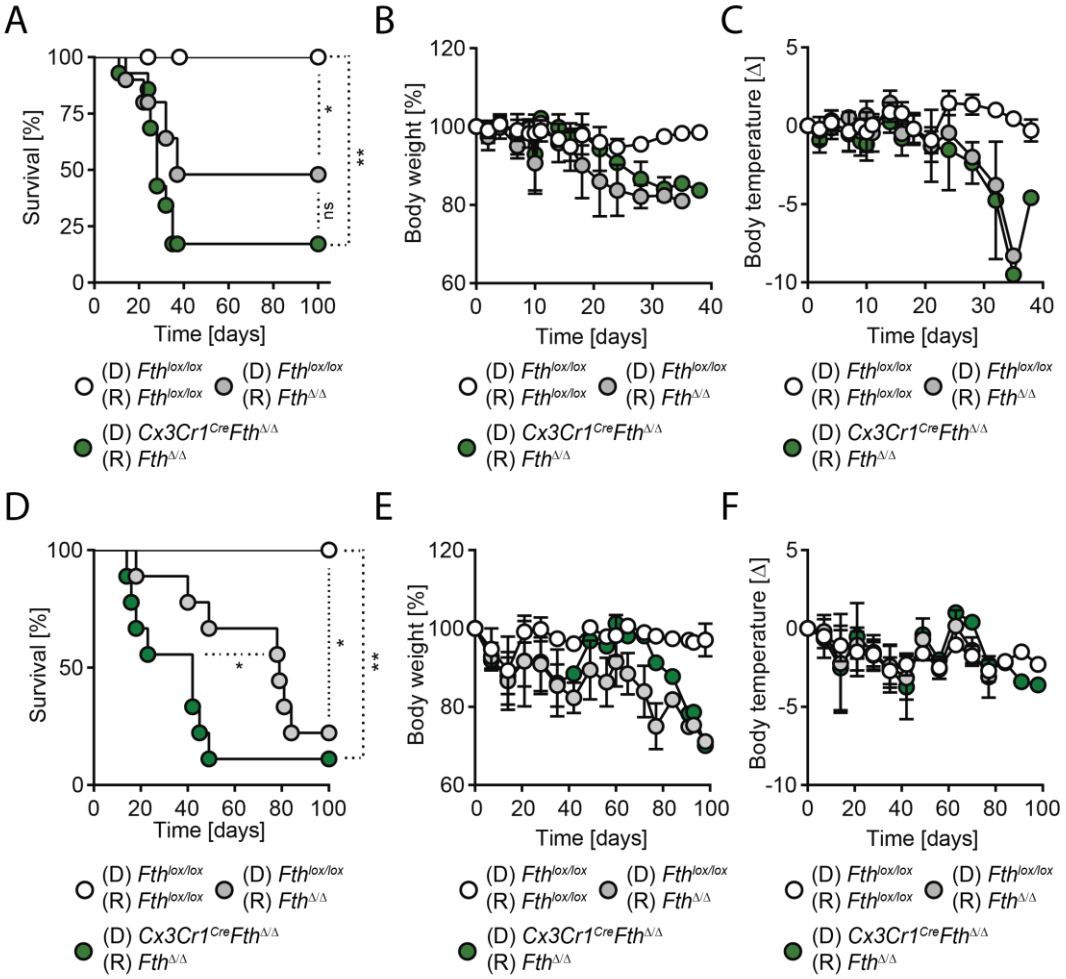

Figure 3.8. *Fth* deletion in CX$_3$CR1$^+$ monocytes/macrophages. A) Survival curve of *Cx$_3$cr1*$^{CreER\text{-}T2}$*Fth*$^{\Delta/\Delta}$→*R26.Fth*$^{\Delta/\Delta}$ (n=11) and control *Fth*$^{lox/lox}$→*Fth*$^{lox/lox}$ (n=5) and *Fth*$^{lox/lox}$→*R26.Fth*$^{\Delta/\Delta}$ (n=7) mice after deletion with a prolonged administration of Tamoxifen by oral gavage (1mg of Tamoxifen/mouse for 2 times a week during 3 weeks). Body weight and temperature of these mice is presented in B) and C) respectively. D) Survival curve of *Cx3cr1*$^{CreER\text{-}T2}$*Fth*$^{\Delta/\Delta}$→*R26.Fth*$^{\Delta/\Delta}$ (n=5) and control *Fth*$^{lox/lox}$→*Fth*$^{lox/lox}$ (n=2) and *Fth*$^{lox/lox}$→*R26.Fth*$^{\Delta/\Delta}$ (n=6) after deletion with Tamoxifen food. Mice were exposed to Tamoxifen food (360mg/kg) twice for one week, interrupted by one week of standard food. Body weight and temperature of these mice is presented in E) and F), respectively. *P<0,05, **P<0,005, ***P<0,001.

3.4. Generation and characterization of a transgenic tagged-FTH protein.

Macrophages can secrete ferritin (Cohen et al., 2010) which is then transferred to tissues as an additional mechanism of Fe distribution and recirculation (Cohen et al., 2010; Meyron-Holtz et al., 2011). To assess if this process was active *in vivo* and eventually responsible for the survival of $Fth^{lox/lox}$→$R26.Fth^{\Delta/\Delta}$ mice, the host laboratory generated a transgenic mouse model in which FTH was tagged with a 14 amino-acid V5 peptide derived from the RNAa (alpha) subunit of the simian parainfluenza virus type 5 (Southern et al., 1991), henceforth referred to as V5 (Figure 3.9A). For this purpose, genetic modification of the *Fth* locus was achieved by CRISPR/Cas9 technology, a highly efficient methodology for genetic manipulation (Jinek et al., 2012). Briefly, bacterial Cas9 nuclease along with a specifically engineered guide RNA can be targeted to cleave any double strand DNA sequence of interest as long as there is recognition of the targeted DNA sequence by the guide RNA (Jinek et al., 2012). These, along with a protospacer adjacent motif (PAM), were the only necessary components to induce Cas9 mediated cleavage of the DNA sequences (Mali et al., 2013). This allows for highly efficient and precise gene editing (Wang et al., 2013; Yang et al., 2013). Thus, Cas9 mRNA, specific single-guide RNA (sgRNA) targeting the 5' end of the *Fth* gene and a corresponding oligo, containing the V5 sequence flanked by sequences homologous to the insertion site, were co-injected into mouse zygote cells. DNA cleavage by the Cas9 enzyme induced the cell autonomous homology directed repair (HDR) mechanisms, leading to homologous recombination and in some cases the incorporation of the V5 containing oligo into the DNA sequence. (Figure 3.9A). The insertion of the tag in the N-terminus of FTH was chosen over the C-terminus since the N-terminus of FTH extends outwards, from the protein cage complex and does not play a role in protein-protein interactions (Zhang and Orner, 2011). After injection, the blastocysts were transplanted into foster mothers (Figure 3.9B) and pups were born 21 days later.

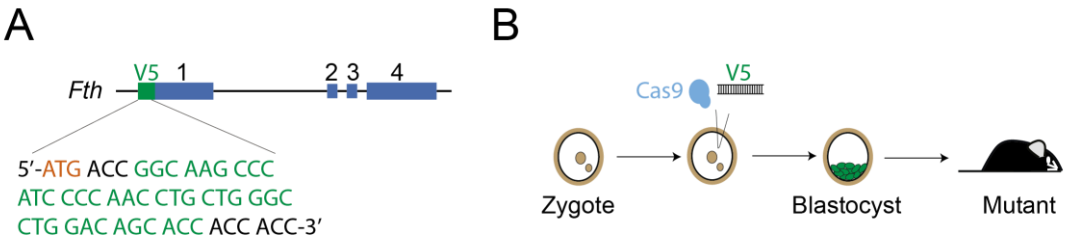

Figure 3.9. Generation of V5-FTH mice by CRISPR/Cas9. A) Schematic representation of the V5 insertion on the *Fth* gene locus. Orange letters represent the start codon ATG of the *Fth* gene and the DNA sequence of the V5 epitope is shown in green. Diagram also depicts overall structure of the *Fth* gene locus. Exons are represented as blue boxes and introns as the space between the assorted exons. B) Generation of mice with the V5 insertion through targeted mutation by the CRISPR/Cas9 system. Cas9 mRNA, sgRNA and V5 oligonucleotides were inserted into fertilized eggs, after formation of the blastocyst the embryos were transferred into foster mothers. Courtesy of Birte Blankenhaus.

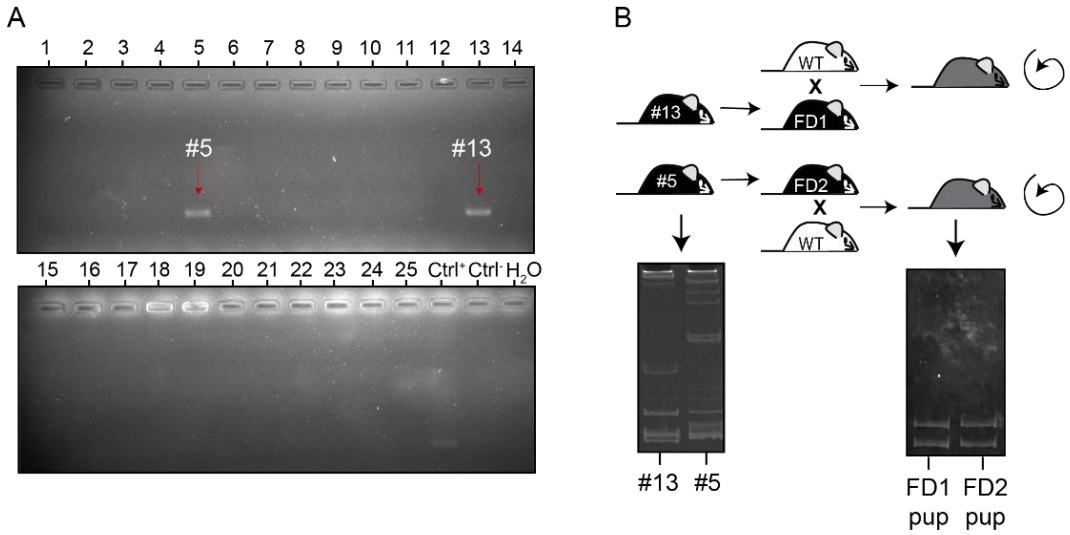

Figure 3.10. Identification and breeding of V5 positive mice after CRISPR/Cas9. A) V5 screening by PCR using V5 forward and FTH reverse primers to genotype genetically modified pups. Two mice (#5 and #13) showed positive bands for the V5 insertion. B) Breeding strategy used to obtain V5-FTH mice on a pure C57BL/6 background. Female #5 and male #13 were appointed FD1 (Founder 1) and FD2 (Founder 2), respectively, and were crossed with WT mice to obtain two pure heterozygous V5 lines. Each PCR represents the genotyping of the FTH locus in each of the V5 mice depicted above. Circular arrows represent intercrossing of littermates with each other.

After birth, V5 screening by PCR allowed the identification of two positive V5 mice that were named #5 and #13 (Figure 3.10A). The V5-tagged mice were able to survive and showed no apparent visible disadvantage compared to normal mice arguing for a functional FTH protein which otherwise would result in embryonic lethality (Ferreira et al., 2000). Further PCR analysis using a polyacrylamide gel for improved resolution of the DNA bands, showed that both mice, the original male #13 and female #5 were heterozygous for *Fth* and in addition present bands that might be the result of off-target events occurring during the recombination process or modifications of the second *Fth* allele. (Figure 3.10B). To generate V5-*Fth* mice on a clean B6 background male #13 (founder 1) and female #5 (founder 2) were crossed with C57BL/6 mice to generate heterozygous progeny containing the tagged *V5-Fth* and an *Fth* wild type allele (Figure 3.10B). These mice were then crossed with littermates to produce V5 heterozygous ($Fth^{wt/V5}$) and V5 homozygous ($Fth^{V5/V5}$) progeny.

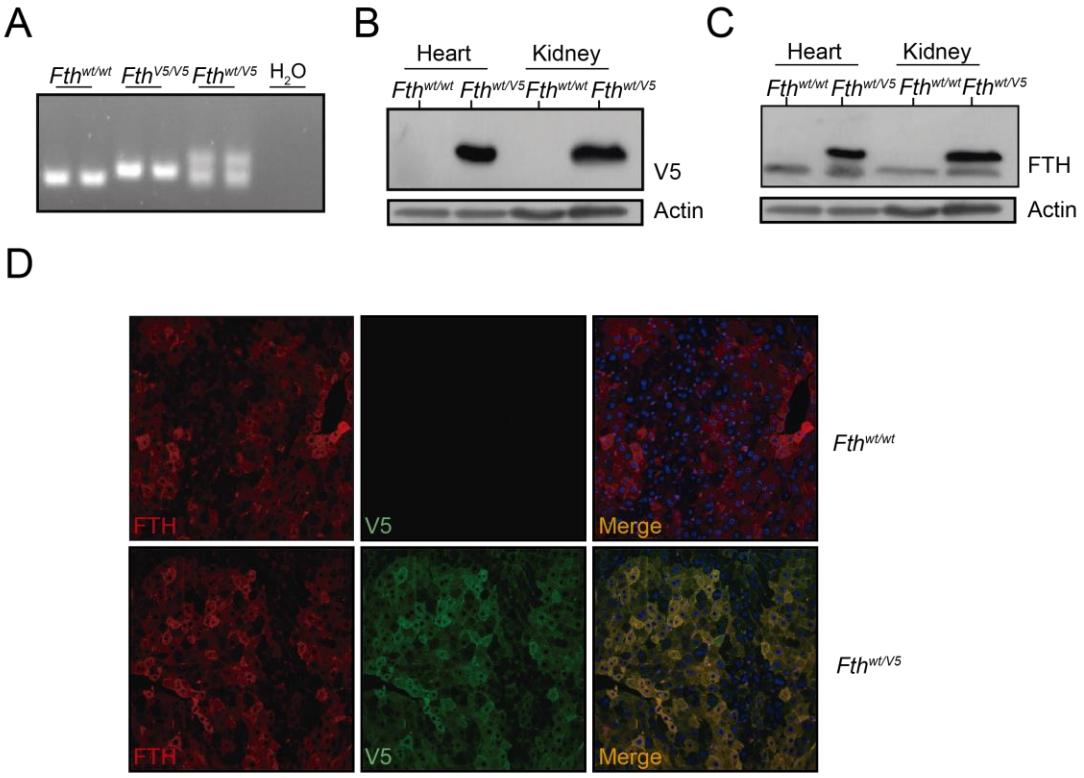

Figure 3.11. Identification of V5 sequence and protein by PCR, western blot and immunofluorescence. A) Representative PCR from *Fth* screening of mice obtained from the breeding of one of the two heterozygous crossings. V5 identification is easily distinguished from wild type mice (*Fth*$^{wt/wt}$) by the different molecular weight caused by the added V5 tag on one of the *Fth* alleles (*Fth*$^{wt/V5}$) or both *Fth* alleles (Fth$^{V5/V5}$). V5 epitope (B) and FTH (C) staining by western blot in heart and kidney extracts of C57BL/6 wild type and *Fth*$^{wt/V5}$ mice. B-actin was used has loading control. D) Representative immunostaining of liver sections of *Fth*$^{wt/wt}$ and *Fth*$^{wt/V5}$ mice. Staining's for FTH (red), V5 (green) and DNA (blue) are shown in C57BL/6 (D, top panel) and *Fth*$^{wt/V5}$ (D, bottom panel) mice under homeostatic conditions. Merge panels show overlay of FTH (red), V5 (green) staining as well as DNA staining by DAPI (not shown).

The *Fth*$^{wt/V5}$ and *Fth*$^{V5/V5}$ mice could be distinguished from wild type (*Fth*$^{wt/wt}$) mice and within themselves by PCR (Figure 3.11A). It was also possible to identify the V5 epitope by western blot using anti-V5 Abs (Figure 3.11B). Due to the difference in molecular weight, i.e. about 1kDa added by the fusion of the V5 peptide, it was also possible to visualize two bands in heterozygous mice, when using anti-FTH Abs showing the distinction between the lighter wild type FTH proteins from the heavier V5-FTH fusion proteins (Figure 3.11C). Finally, we further tested the localization of the V5-FTH protein by immunofluorescence staining in liver sections (Figure 3.11D). Liver sections from wild type C57BL/6 mice showed no signal for the V5-tag, although a strong FTH signal was detected (Figure 3.11D, top panel). In V5-tagged mice, FTH and V5 stainings overlapped confirming the success of the CRISPR-Cas9 strategy (Figure 3.11D, bottom panel).

3.5. FTH is not delivered by macrophages to parenchyma tissues.

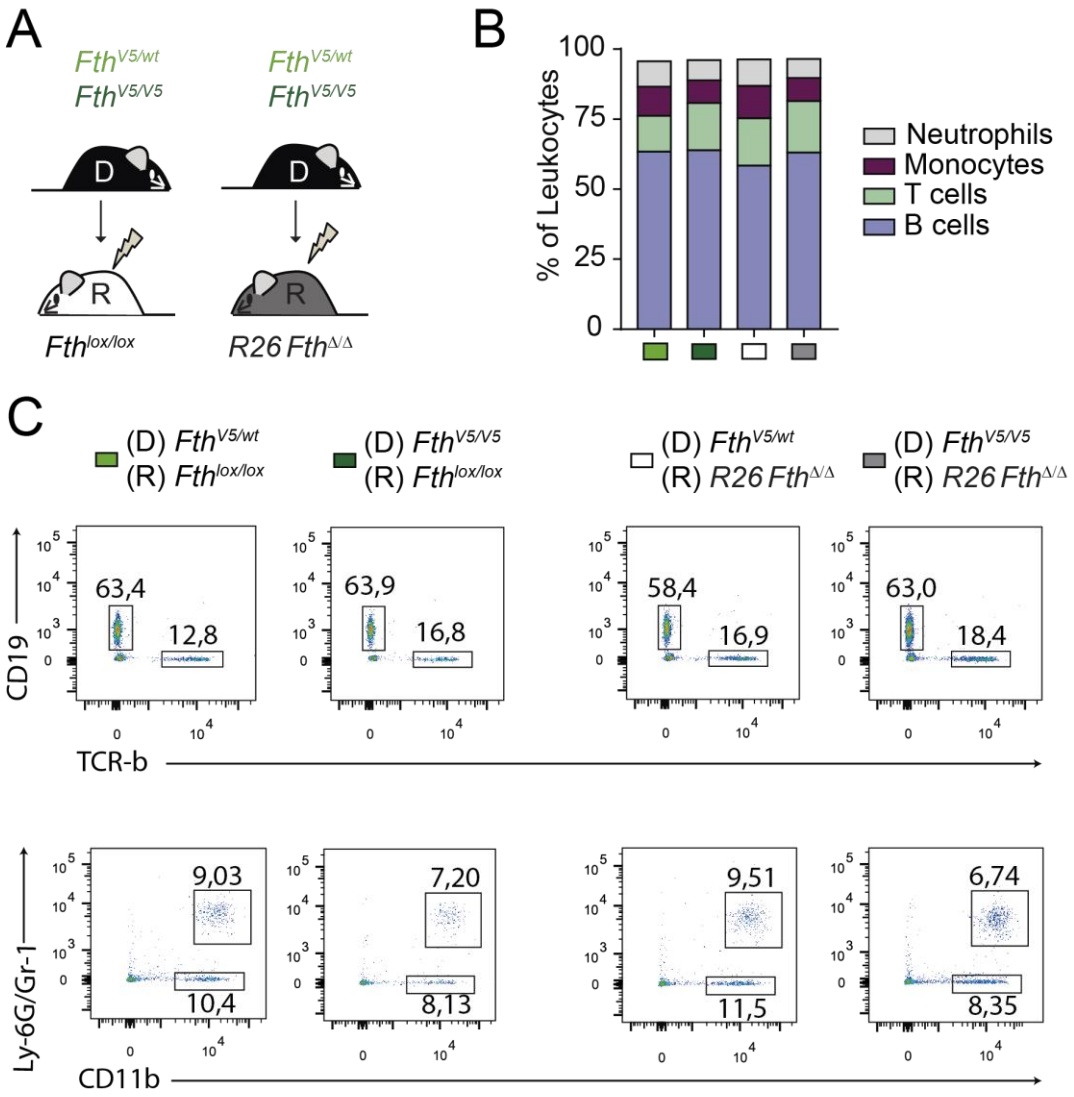

Figure 3.12. Reconstitution by V5-*Fth* bone marrow. A) Schematic representation of the generation of V5^{heterozygous} (*Fth*$^{wt/V5}$) and V5^{homozygous} (*Fth*$^{V5/V5}$) chimeric mice. V5-*Fth* bone marrow was collected from donor mice and administered to *Fth*$^{lox/lox}$ and *R26*$^{CreER\text{-}T2}$*Fth*$^{\Delta/\Delta}$ recipient mice. B) Relative percentage of leukocytes in each of the four groups after reconstitution. C) Representative FACS plots for the analysis of leukocyte populations in bone marrow chimeric mice. Monocytes, Neutrophils, T and B cell populations were identified using CD11b, Ly-6G/Gr-1, TCR-b and CD19 Abs, respectively.

To investigate whether FTH transits from macrophages to parenchyma cells, when parenchyma cells lack *Fth* expression, lethally irradiated *Fth*$^{lox/lox}$ and *R26.Fth*$^{\Delta/\Delta}$ mice were transplanted with bone marrows from *Fth*$^{wt/V5}$ *and Fth*$^{V5/V5}$ mice (Figure 3.12A). Bone marrow reconstitution was confirmed by flow cytometry. Relative numbers of circulating monocytes, neutrophils, T and B cells in *Fth*$^{V5/V5}$→*Fth*$^{lox/lox}$ and *Fth*$^{V5/V5}$→*R26.Fth*$^{\Delta/\Delta}$ mice were similar to those of *Fth*$^{lox/lox}$→*Fth*$^{lox/lox}$ or *Fth*$^{lox/lox}$→*R26.Fth*$^{\Delta/\Delta}$ chimeric mice (Figure 3.12B, C).

No differences in survival were registered (Figure 3.13A), after deletion by Tamoxifen as well as normal ranges of weight (Figure 3.13B) and temperature (Figure 3.13C) showing that the V5-*Fth* bone marrow cells keep their ability to rescue *R26.Fth*$^{\Delta/\Delta}$ hosts.

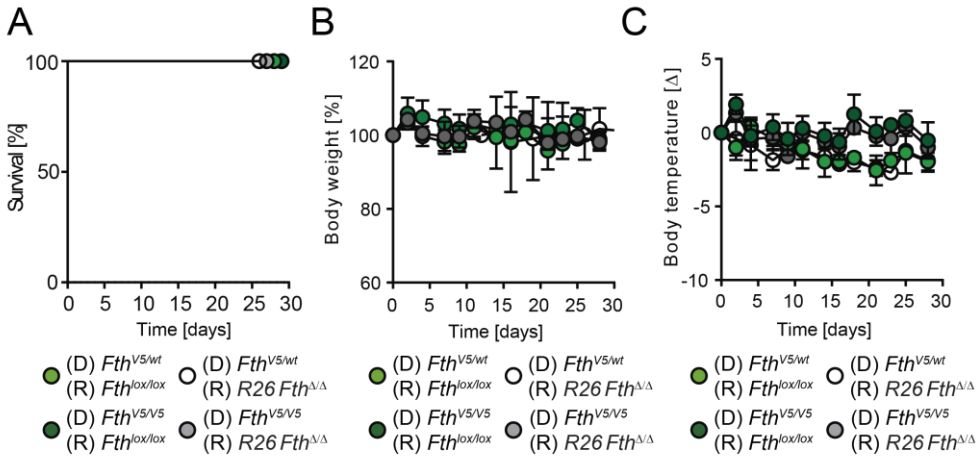

Figure 3.13. Survival, body weight and temperature curves of V5-*Fth* chimeric mice A) Survival curve from both *Fth*$^{wt/V5}$→*Fth*$^{\Delta/\Delta}$ (n=3), *Fth*$^{V5/V5}$→*Fth*$^{\Delta/\Delta}$ (n=4) and controls *Fth*$^{wt/V5}$→*Fth*$^{lox/lox}$ (n=2) and *Fth*$^{V5/V5}$→*Fth*$^{lox/lox}$ (n=3) groups showing no differences 30 days of deletion (1mg/mouse of Tamoxifen by oral gavage 3 times in the course of one week). Bodyweight and temperature of these mice is presented in B) and C) respectively.

To test whether macrophages could actively deliver FTH to tissues, either in normal or *Fth*-deleted conditions, we detected the V5-FTH fusion protein by immunofluorescent imaging in livers of chimeric animals. For accurate identification of tissue macrophages, Abs directed against F4/80 were tested in the liver of wild type mice using a previously described immunofluorescence protocol on paraffin sections (Figure 3.11D). Unfortunately, it was not possible to obtain a positive staining for F4/80 using this experimental setup (Figure 3.14).

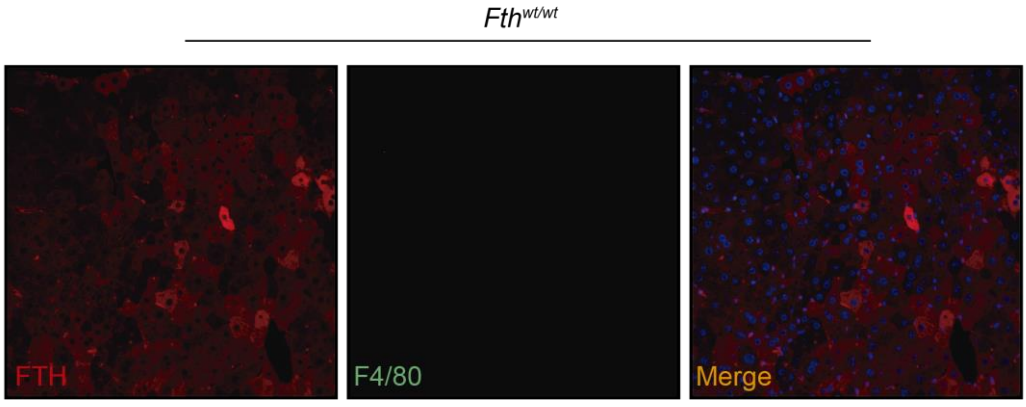

Figure 3.14. F4/80 staining in paraffin section. Representative immunostaining of liver sections stained with FTH (red) and F4/80 (green) antibodies in a C57BL/6 wild type mouse. No signal for F4/80 was obtained. Merge panel shows overlay of FTH and F4/80 with staining for DNA using DAPI (blue).

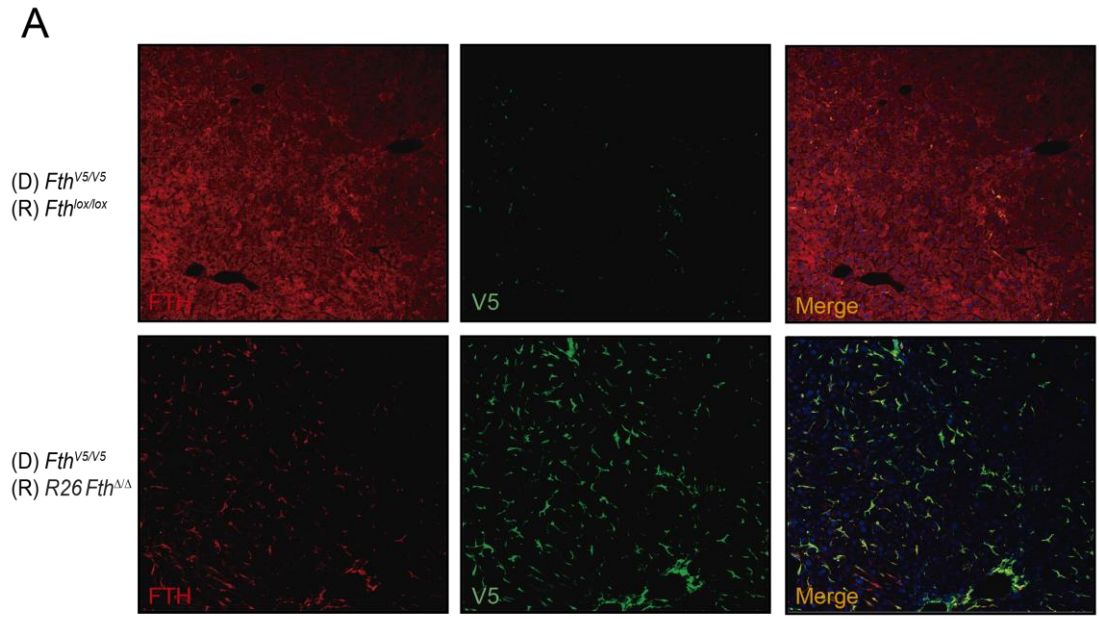

Figure 3.15. FTH and V5-FTH detection in liver sections. Representative whole-mount immunostaining showing FTH (red) and V5 (green) expression in the liver of *Fth*$^{V5/V5}$→*Fth*$^{lox/lox}$ (top panel) and *Fth*$^{V5/V5}$→*Fth*$^{\Delta/\Delta}$ (bottom panel) mice. The right panel in each row shows the overlay (merge) of FTH and V5 together with the DAPI staining for DNA (blue).

Therefore, a different protocol was employed which involved fixation of the organs with 4% PFA followed by tissue embedding in low melting agarose. Thicker sections of the liver were also cut as described in (Cardoso et al., 2017). Abs directed against CD68, a well-established macrophage marker (Holness et al., 1993) were also utilized. Using this strategy, we found that *Fth*$^{V5/V5}$→*Fth*$^{lox/lox}$ mice showed a normal staining for FTH in the tissues, i.e. mainly hepatocytes and some interstitial immune cells most likely Kupffer cells. Interestingly, V5 staining was restricted to F4/80^{+} and CD68^{+} macrophages (Figure 3.15A). There was no FTH staining in hepatocytes from *Fth*$^{V5/V5}$→ *R26.Fth*$^{\Delta/\Delta}$ mice (Figure 3.15A). Instead, a strong staining of FTH could be detected in cells that were morphologically similar to Kupffer cells (Figure 3.15). Similarly, no V5 staining was found in hepatocytes whereas V5 expression was also detected in F4/80^{+} and CD68^{+} cells (Figure 3.16). In fact, both F4/80^{+} (Figure 3.16A) and CD68^{+} (Figure 3.16B) macrophages accumulated in larger numbers in FTH-depleted tissues than in FTH competent tissues (Fig 3.16A, B). In addition, these cells show a strong V5 staining, indicating recruitment and infiltration of bone marrow derived monocytes into the tissues, rather than proliferation of resident macrophage populations, in response to *Fth* deficiency. This increased expression of V5 in F4/80^{+} and CD68^{+} cells also indicates the increased expression of FTH in these cells and therefore hints to a compensatory mechanism that these cells employ in order to detoxify the tissues from otherwise deleterious iron concentrations (Figure 3.16A, B).

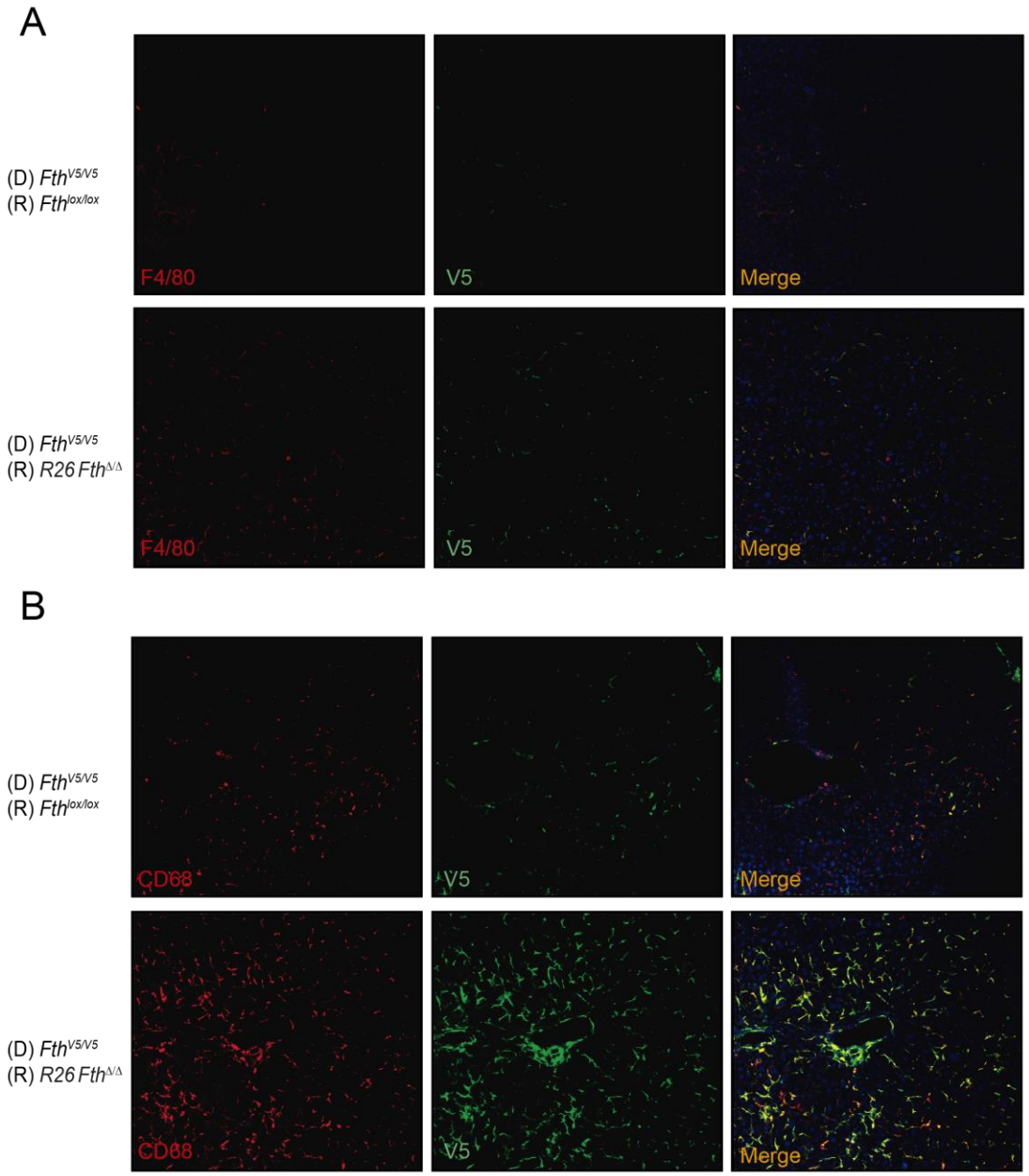

Figure 3.16. F4/80, CD68 and V5-FTH detection in liver sections. Representative whole-mount immunostaining showing A) F4/80 (red) + V5 (green) and B) CD68 (red) + V5 (green) expression in the liver of *Fth*$^{V5/V5}$→*Fth*$^{lox/lox}$ (top panel) and *Fth*$^{V5/V5}$→*R26.Fth*$^{\Delta/\Delta}$ (bottom panel) mice. The genotypes are shown side by side and the last panel in each rectangle (indicated as "Merge") shows the overlay of the two other channels along with the DAPI staining.

Altogether, these data demonstrate that FTH does not transit from macrophages to parenchyma cells at steady state or in a situation where parenchyma cells lacks *Fth* expression. Moreover, macrophages seem to upregulate *Fth* when parenchyma cells lack *Fth* expression. Presumably macrophages react to the lack of *Fth* expression in parenchyma tissue, most likely contributing to maintain tissue iron homeostasis and avoid Fe-driven oxidative stress that otherwise compromises systemic homeostasis.

4. Discussion

Ferritin is an important regulator of intracellular Fe homeostasis, limiting Fe-assisted ROS generation via the Fenton reaction. Constitutive deletion of *Fth* in mice is embryonically lethal and therefore lack of *Fth* expression can be incompatible with life (Ferreira et al., 2000). Interestingly, conditional *Fth* deletion in liver and leukocytes leads to liver dysfunction and damage but not to death (Darshan et al., 2009). To investigate the effects of global *Fth* deletion in adult mice we used the $R26^{CreER\text{-}T2}Fth^{lox/lox}$ (*R26.Fth*$^{\Delta/\Delta}$) mice that allow for temporal control of *Fth* deletion, circumventing embryonic lethality associated with germline encoded deletion. We confirmed that Tamoxifen induced a global repression of *Fth* mRNA in all the tissues of *R26.Fth*$^{\Delta/\Delta}$ mice (Figure 3.2A). Of note, the brain of *R26.Fth*$^{\Delta/\Delta}$ mice had about 70% reduction of *Fth* mRNA expression, as compared to control $Fth^{lox/lox}$ mice. Since *R26* is an ubiquitous promoter and Tamoxifen can effectively penetrate the blood-brain barrier and access brain tissue (Hayashi and McMahon, 2002), we speculate that the higher levels of FTH expression in this organ are due to increased Tamoxifen degradation in the brain of adult mice (Valny et al., 2016).

These results represent an improvement in terms of achieving global *Fth* deletion, over previous studies using a Cre recombinase system under the Mx dynamin-like GTPase 1 (Mx1) promoter (Darshan et al., 2009). In this study, the authors reported *Fth* deletion in the spleen, liver and bone marrow, but not in the heart, kidney and lung. Although the *Mx1* promoter is present in virtually all cell types, its activation is under the control of type I interferon (alpha and beta) signaling and can be strongly activated by Poly-IC, a double stranded RNA analog recognized by TLR3 and potent interferon inducer (Kuhn et al., 1995). However, deletion efficiency shows high variability in some organs, and only the liver and hematopoietic organs show efficient *Fth* deletion (Darshan et al., 2009), possibly due to stronger interferon responses in these tissues or overall interferon availability (Kuhn et al., 1995). Therefore, the mice generated in our study represent a more robust system to study total deletion of *Fth*. To further test if *Fth* deletion was reflected at the protein level, we monitored the levels of *Fth* protein expression in heart, kidneys, lungs and liver of deleted mice by western blot (Figure 3.2B-E). We confirmed that *Fth* can be successfully deleted in *R26.Fth*$^{\Delta/\Delta}$ *vs.* control $Fth^{lox/lox}$ mice, except in the kidney (Figure 3.2D) where one of the *R26.Fth*$^{\Delta/\Delta}$ mice expressed very high levels of FTH, likely owed to defective *Fth* deletion.

FTH protein levels in the heart of *R26.Fth*$^{\Delta/\Delta}$ *vs.* control $Fth^{lox/lox}$ mice are not reduced to the same extent as compared to the mRNA levels (Figure 3.2A). Presumably this is due to a higher FTH protein stability owed to lower turnover due to decreased protein degradation or due to a post-transcriptional mechanism that would be activated to compensate for low levels of *Fth* mRNA.

Having assessed the efficiency of *Fth* deletion in these mice, the next step was to characterize their phenotype. Upon Tamoxifen administration, *R26.Fth*$^{\Delta/\Delta}$ mice lost body weight and temperature (Figure 3.3A, B), succumbing within 16 days (Figure 3.3C). In addition, these mice also showed high levels of tissue damage, oxidative stress and heart dysfunction (Birte Blankenhaus, unpublished data). This was not due to Tamoxifen administration *per se*, since tissue damage was not observed in control *Fth*$^{lox/lox}$ mice that received Tamoxifen at the same dosage and schedule. This suggests that ferritin is essential to support homeostasis during adulthood.

Given that macrophages are thought to play an important role in the maintenance of Fe metabolism (Soares and Hamza, 2016), we hypothesized that *Fth* expression by macrophages may be essential to support homeostasis during adulthood. We tested this hypothesis using chimeric mice in which *Fth* expression is restricted to hematopoietic *vs.* parenchyma cells. Surprisingly, reconstitution of *R26.Fth* $^{\Delta/\Delta}$ mice with bone marrow cells from *Fth*$^{lox/lox}$ mice expressing *Fth* rescued Tamoxifen-induced loss of body weight and temperature and more importantly the lethality associated with *Fth* deletion in the parenchyma cells of chimeric *Fth*$^{lox/lox}$→*R26.Fth*$^{\Delta/\Delta}$ mice (Figure 3.4B). In contrast reconstitution of *R26.Fth*$^{lox/lox}$ mice with bone marrow from *LysM*^{Cre}*Fth*$^{\Delta/\Delta}$ mice failed to rescue Tamoxifen-induced loss of body weight, temperature and lethality associated with *Fth* deletion in the parenchyma cells of chimeric *LysM*^{Cre}*Fth*$^{\Delta/\Delta}$→*R26.Fth*$^{\Delta/\Delta}$ mice (Figure 3.4B). Moreover, western blot analysis showed that an important proportion of FTH protein expression in these mice derives from the myeloid compartment (Figure 3.5A-D). This is particularly evident for the liver (Figure 3.5A), kidneys (Figure 3.5C) and lungs (Figure 3.5D) of *LysM*^{Cre}*Fth*$^{\Delta/\Delta}$→*R26.Fth*$^{\Delta/\Delta}$ *vs.* *Fth*$^{lox/lox}$→*R26.Fth*$^{\Delta/\Delta}$ mice with *LysM*^{Cre}*Fth*$^{\Delta/\Delta}$ →*R26.Fth*$^{\Delta/\Delta}$ mice having a reduced level of FTH protein expression as compared to *Fth*$^{lox/lox}$→*R26.Fth*$^{\Delta/\Delta}$ mice (Figure 3.2B-E). This likely explains the lethality of chimeric *LysM*^{Cre}*Fth*$^{\Delta/\Delta}$→*R26.Fth*$^{\Delta/\Delta}$ *vs*. *Fth*$^{lox/lox}$→*R26.Fth*$^{\Delta/\Delta}$ mice. Further, *Fth*$^{lox/lox}$→*R26.Fth*$^{\Delta/\Delta}$ mice showed an overall 60% decrease of FTH levels in the heart, while FTH expression in the hearts of *LysM*^{Cre}*Fth*$^{\Delta/\Delta}$→*R26.Fth*$^{\Delta/\Delta}$ mice drops more than 80%, as compared to the levels of FTH expression in the hearts of control *Fth*$^{lox/lox}$→*Fth*$^{lox/lox}$ mice.

Given the high level of sensitivity of cardiomyocytes to Fe toxicity (Nairz et al., 2017) and the important role played by macrophages in maintaining cardiac function (Nahrendorf and Swirski, 2016; Hulsmans et al., 2017) we conclude that FTH expression in macrophages that populate the heart cannot drop below a certain level, without compromising organismal homeostasis. It is also possible that a different hematopoietic-derived cell population might supply the heart with FTH. Of note, Tamoxifen-induced *Fth* deletion in the heart is not as effective as in other tissues, as illustrated by residual levels of *Fth* mRNA after Tamoxifen administration to *R26.Fth* $^{\Delta/\Delta}$ mice (Figure 3.2A).

Overall these results suggest that while most of the tissue ferritin comes from parenchyma cells, mice lacking *Fth* expression in parenchymal cells can survive provided that myeloid cells express *Fth*. However, *Fth* deletion in parenchyma cells becomes lethal when *Fth* expression is also deleted from myeloid cells, as illustrated for the lethality of chimeric $LysM^{Cre}Fth^{\Delta/\Delta}\rightarrow R26.Fth^{\Delta/\Delta}$ *vs*. $Fth^{lox/lox}\rightarrow R26.Fth^{\Delta/\Delta}$ mice (Figure 3.4B). This is in line with previous studies showing that lack of *Fth* expression in parenchyma tissues can lead to increased accumulation of labile Fe and consequently ROS formation, as illustrated for intestinal epithelial cells (Vanoaica et al., 2010) as well as hepatocytes (Darshan et al., 2009). Moreover, macrophages have also been shown to contribute in reducing muscle damage by a mechanism involving the upregulation of *Fth* (Corna et al., 2016).

Having established that expression of *Fth* by myeloid cells can compensate for the lack of *Fth* expression in parenchyma tissues (Figure 3.4B) we asked what would be the specific myeloid-derived population involved. Although the relative contribution of different monocyte subsets to the overall composition of tissue resident macrophages remains unclear (Kierdorf et al., 2016) several studies suggest that blood circulating monocytes can replace tissue-resident macrophages, when these are deleted following damage or infection (Blériot et al., 2015; Bruttger et al., 2015). This requires that monocytes migrate from the bone marrow and infiltrate tissues, via a CCR2-dependent mechanism, likely involving the chemokine monocyte chemoattractant protein-1 (MCP-1, also known as CCL2) (Serbina and Pamer, 2006; Tsou et al., 2007; Varol et al., 2015). When lethally irradiated $R26.Fth^{\Delta/\Delta}$ mice were reconstituted with bone marrow from $Ccr2^{-/-}$ mice there was a decrease in body weight (Figure 3.6C) and temperature (Figure 3.6D) as well as reduced survival of chimeric $Ccr2^{-/-}\rightarrow R26.Fth^{\Delta/\Delta}$ mice, as compared to $Fth^{lox/lox}\rightarrow R26.Fth^{\Delta/\Delta}$ mice (Figure 3.6B). This effect was only observed after a more extended time span, as compared to chimeric $LysM^{Cre}Fth^{\Delta/\Delta}\rightarrow R26.Fth^{\Delta/\Delta}$ mice (Figure 3.4B), which succumbed within 40 days of Tamoxifen administration. We conclude that a while $Ccr2^{+}$ monocytes expressing *Fth* are important to maintain homeostasis there is probably a subset of monocytes that migrates into damaged tissues independently of *Ccr2* expression and signaling, where they mitigate tissue damage, likely by sustaining residual *Fth* activity *in situ*. This conclusion is also supported by a previous report showing that the spleen acts as a reservoir for a specific subset of monocytes which are able to migrate to, and infiltrate damaged tissues independent of *Ccr2* signaling (Swirski et al., 2009). Unfortunately, experiments using splenectomized mice aimed at testing this hypothesis failed to generate conclusive data, due to technical constrains (Figure 3.7A). Therefore, further investigation is required to clarify our hypothesis.

Despite intensive investigation, macrophage ontogeny remains controversial. The prevalent theory for several decades was that macrophages develop exclusively from circulating monocytes (van Furth, 1976). However, recent reports have shown that tissue-resident macrophages are established before birth (Samokhvalov et al., 2007; Hoeffel et al., 2012; Gomez Perdiguero et al.,

2014). With the exception of microglia and intestinal macrophages, tissue-resident macrophage progenitors migrate and establish populations in fetal tissues before birth via a mechanism that requires *Cx3cr1* expression (Yona et al., 2013). Moreover, a subset of monocytes expressing high levels of *Cx3cr1* has been identified (Geissmann et al., 2003) and shown to migrate from the bone marrow to adult tissues where they act as precursors for tissue-resident macrophages, differentiating into various specialized macrophage subtypes (Geissmann et al., 2003). However, regardless of their origin, tissue-resident macrophages have self-renewable capabilities which are mainly independent from circulating monocytes (Hashimoto et al., 2013).

With the objective of understanding the contribution of tissue-resident macrophages in the rescue of *R26.Fth*$^{\Delta/\Delta}$ mice, two different strategies were used to delete *Fth* in chimeric *Cx3Cr1*$^{\text{CreER-T2}}$*Fth*$^{\Delta/\Delta}$→*R26.Fth*$^{\Delta/\Delta}$ mice. The first one involved continuous Tamoxifen administrations during three weeks (Figure 3.8A-C) and the other involving continuous Tamoxifen administration in food (Figure 3.8D-F). The side effects of Tamoxifen administration is a widely recognized complication of the inducible Cre$^{\text{ER-T2}}$ system and has been associated with tissue damage in mice (Huh et al., 2012; Gao et al., 2016). Deletion of *Fth* in chimeric *Cx3Cr1*$^{\text{CreER-T2}}$*Fth*$^{\Delta/\Delta}$→*R26.Fth*$^{\Delta/\Delta}$ mice was associated with lethality using both Tamoxifen strategies. This was also the case for *Fth*$^{\text{lox/lox}}$→*R26.Fth*$^{\Delta/\Delta}$ mice, which undermines the interpretation of the results. Considering the already deleterious modifications performed on the recipient animals due to irradiation, one reason these animals fail to survive could be due to their increased susceptibility to tissue damage owing to a more stringent Tamoxifen regime. Another possible explanation is that the increased Tamoxifen administration regimen could lead to complete *Fth* deletion in the brain. This is consistent with the observation that the same regimes of Tamoxifen administration are not lethal to control *Fth*$^{\text{lox/lox}}$→*Fth*$^{\text{lox/lox}}$ mice. One way this technical problem could be circumvented is by using *Cx$_3$cr1*$^{\text{Cre}}$*Fth*$^{\text{lox/lox}}$ animals where *Fth* is constitutively deleted from *Cx$_3$cr1*$^{+}$ cells, allowing to compare under low Tamoxifen regimen the outcome of *Fth* deletion in *Cx3Cr1*$^{\text{Cre}}$*Fth*$^{\Delta/\Delta}$→*R26.Fth*$^{\Delta/\Delta}$ *vs. Fth*$^{\text{lox/lox}}$→*R26.Fth*$^{\Delta/\Delta}$ mice. These experiments are underway.

Although the use of *Cx3Cr1*$^{\text{CreER-T2}}$*Fth*$^{\Delta/\Delta}$ mice as bone marrow donors did not generate conclusive results, the data generated with *Ccr2*$^{-/-}$ mice showing that monocyte migration into parenchyma tissues is required to sustain survival (Figure 3.6B), strongly points towards a role of tissue macrophages to compensate the loss of *Fth* expression by the parenchyma cells. This is in accordance with recent reports showing that macrophage migration to parenchyma tissues alleviates Fe-related tissue damage and inflammation (Bolisetty et al., 2015; Corna et al., 2016; Theurl et al., 2016).

Under homeostatic conditions, macrophages can secrete ferritin into circulation acting as the main source of serum ferritin (Cohen et al., 2010). This mechanism has been proposed as an alternative strategy for Fe delivery into tissues (Meyron-Holtz et al., 2011). In *vitro* studies also

showed that in the absence of transferrin, macrophage secreted ferritin is taken up by cultured erythroid precursor cells and used as a source of Fe in erythroid development (Leimberg et al., 2008). I*n vitro* experiments have also shown that ferritin released from Kupffer cells have a high Fe content and can be internalized by hepatocytes (Sibille et al., 1988). In keeping with these findings a FTH receptor has been identified in mice, enabling FTH internalization by endocytosis by hepatocytes, kidney epithelial cells as well as in B and T cells (Chen et al., 2005). Moreover, ferritin can be associated with microtubules in a wide range of cells (Hasan et al., 2006; Infante et al., 2007) which could hint that a mechanism for intracellular ferritin trafficking exists that allows its mobilization after internalization. To further investigate the mechanism supporting the survival of $Fth^{lox/lox} \rightarrow R26.Fth^{\Delta/\Delta}$ mice, the host laboratory generated transgenic mice in which endogenous FTH is fused to a V5 tag peptide (Figure 3.9A). This strategy allowed determining the origin of FTH according to detection of the V5 tag. With this purpose, we tracked V5-FTH expression in $Fth^{V5/V5} \rightarrow Fth^{lox/lox}$ mice, to assess whether secreted FTH is transferred from the hematopoietic compartment into parenchyma cells *in vivo*. Since ferritin is a large multimeric structure composed of two different subunits there was the possibility that the insertion of the V5 tag would interfere with the self-assembly process of the multimeric complex. While it has been shown that small deletions in both N and C terminus of recombinant human FTH did not interfere with this self-assembly or ferroxidase ability (Levi et al., 1988), the effects of the fusion of the mouse FTH protein with a V5 peptide have never been assessed before. Heterozygous $Fth^{wt/V5}$ or homozygous $Fth^{V5/V5}$ mice were viable and healthy and did not show any apparent phenotype when compared to $Fth^{wt/wt}$ mice (Birte Blankenhaus, unpublished data). This argues strongly for the correct functionality of the V5-FTH tagged protein.

As the V5 tag adds 14 amino acids (aa) to the FTH protein, the *V5-Fth* and the *Fth* alleles can be easily distinguished by PCR (Figure 3.11A) as well as by western blot analysis (Figure 3.11B). Surprisingly, the western blot performed in extracts from heterozygous $Fth^{wt/V5}$ mice, using an anti-FTH Ab (Figure 3.11C) showed a different intensity on the upper *vs.* the lower molecular weight FTH band, which corresponds to the V5-FTH tagged *vs.* the endogenous FTH protein. This suggests that V5 may interfere with FTH protein expression and/or ferritin function. Another possible explanation is that the modifications induced by the V5 fusion could increase the affinity of the anti-FTH Ab for the tagged protein. Moreover, the V5 tag could cause some structural changes in the ferritin complex, which could make it more stable or less prone to clearance by the degradation machinery. Using a V5-directed Ab on paraffin sections we found complete co-localization of V5 and FTH on livers of V5 transgenic animals (Figure 3.11E), further arguing for the functionality of the tagged FTH protein.

V5-FTH represents an important tool to characterize the ability of FTH to transit from the myeloid cells to the parenchyma and to gain a unique insight into the mechanism by which ferritin from myeloid cells provides a physiological advantage to the *Fth* deleted parenchyma tissues.

Both *Fth*$^{wt/V5}$→*R26.Fth*$^{\Delta/\Delta}$ and *Fth*$^{V5/V5}$→*R26.Fth*$^{\Delta/\Delta}$ mice survived to a similar extent to *Fth*$^{lox/lox}$→*R26.Fth*$^{\Delta/\Delta}$ mice (Figure 3.13A, 4B). This further supports that V5-FTH is fully functional and as such can be used as a tool to dissect the ability of FTH to transit between compartments. In order to answer which mechanism is used by myeloid cells to support tissue function in the absence of ferritin we decided to use an immunohistochemistry approach by staining FTH, V5 and a macrophage marker that would confirm or not the transit of the V5-FTH fusion protein into parenchyma cells such as hepatocytes. Macrophage, FTH and V5-FTH co-staining required additional set up of the immunohistochemistry protocol. While Abs against V5 and FTH proteins detected the respective epitopes on paraffin sections (Figure 3.11D), the macrophage marker tested failed to do so (Figure 3.14). Paraffin can interfere with the binding of Abs to their respective epitopes due to the chemical alterations exerted by the fixation methods (Zupančič et al., 2017) and although several antigen retrieval protocols have been developed (Shi et al., 2011), a wide variety of antigens still cannot be properly detected (Zupančič et al., 2017). Therefore, this generated the need for the development of a different strategy. A whole-mount immunohistochemistry protocol was used which was adapted from a previous described protocol (Cardoso et al., 2017) (Figure 3.15 A, B). Using this approach, we found that as expected, FTH protein expression was detected in hematopoietic and parenchyma cells of *Fth*$^{wt/V5}$→*Fth*$^{lox/lox}$ or *Fth*$^{V5/V5}$→ *Fth*$^{lox/lox}$ (Figure 3.14). However, V5 staining was limited to cells that resemble morphologically myeloid infiltrating cells that express F4/80 or CD68, i.e. macrophages (Figure 3.15 A, B). This suggests that when expressed in macrophages FTH does not transit to parenchyma cells in the liver, e.g. hepatocytes. There was no detection of FTH protein in the parenchyma of *Fth*$^{V5/V5}$→*R26.Fth*$^{\Delta/\Delta}$ mice (Figure 3.15). FTH in these mice was limited to few interstitial cells suggesting that FTH does not transit from macrophages to parenchyma cells and instead FTH expression is limited to macrophages. As expected, all the FTH-expressing cells co-express V5 (Figure 3.15), showing that all the expression of FTH is confined to hematopoietic infiltrating cells, i.e. macrophages. Moreover, FTH expressed by tissue macrophages does not transit to parenchyma cells. Instead, there seems to be an accumulation of FTH-expressing tissue macrophages expressing high levels of V5-FTH, probably compensating for the lack of FTH expression in parenchyma cells. Instead, parenchyma cells in these mice up regulate the expression of the Fe exporter FPN (Birte Blankenhaus, unpublished data), possibly to avoid intracellular Fe accumulation. This should generate an increase in extracellular labile Fe, which is probably up taken by macrophages and stored inside Ferritin. In the absence of *Fth*-competent macrophages the extracellular Fe would accumulate and act as a pro-oxidant to cause oxidative damage and tissue dysfunction consequently leading to death. These results go against previous *in vitro* data showing that macrophages can increase FTH secretion under conditions of Fe overload (Yuan et al., 2004) and that hepatocytes (Sibille et al., 1988) or human erythroid precursors (Leimberg et al., 2008) uptake ferritin produced by macrophages. Interestingly, given

that hepatocytes express the FTH receptor T cell immunoglobulin-domain and mucin-domain 2 (TIM-2), which allows for FTH internalization (Chen et al., 2005), no FTH is seen inside these cells under the experimental conditions used herein (Figure 3.15 and Figure 3.16). This argues further that FTH is not secreted by macrophages under these experimental conditions since, as illustrated by the lack of *V5-Fth* expression in parenchyma cells, i.e. hepatocytes. Instead, Fe is likely loaded and stored by *Fth*-expressing macrophages that may then release Fe to be delivered into different tissues via different mechanisms. This hypothesis is in fact supported by several studies that show increased FPN expression in macrophages after Fe clearance, as a mechanism for Fe delivery to tissues (Corna et al., 2016; Theurl et al., 2016).

Altogether these results provide insights into the overall contribution of myeloid cells, i.e. macrophages, to the overall level of *Fth* expression in different tissues. When parenchyma tissues lack or have significantly reduced levels of FTH protein expression bone marrow derived macrophages that infiltrate these tissues up regulate the expression of *Fth*, which is essential to maintain homeostasis and sustain survival. Experiments aimed at determining the specific myeloid population responsible for these effects yielded conflicting results, likely due to technical issues. As such, it remains to be established which specific *Fth*-expressing myeloid subset compensates for the lack of *Fth* expression in parenchyma cells. Finally, the characterization and development of *Fth*-tagged transgenic mouse strain allowed to answer one of the main questions proposed by this thesis, namely, whether macrophages deliver FTH into parenchyma tissues. We found that this is not the case. Furthermore, these transgenic mice can be a useful tool for future experiments aimed at understanding the biologic function of FTH. Our work reinforces the importance of FTH expression in the maintenance of homeostasis.

5. References

Aisen, P., Enns, C., and Wessling-Resnick, M., 2001. Chemistry and biology of eukaryotic iron metabolism. International Journal of Biochemistry and Cell Biology 33(10): 940–959.

Alkhateeb, A. A., and Connor, J. R., 2013. The significance of ferritin in cancer: Anti-oxidation, inflammation and tumorigenesis. Biochimica et Biophysica Acta - Reviews on Cancer 1836(2): 245–254.

Anderson, C., Shen, L., Eisenstein, R., and Leibold, E. a, 2012. Mammalian iron metabolism and its control by iron regulatory proteins. Biochimica et biophysica acta 1823(9): 1468–1483.

Arosio, P., Carmona, F., Gozzelino, R., Maccarinelli, F., and Poli, M., 2015. The importance of eukaryotic ferritins in iron handling and cytoprotection. Biochemical Journal 472(1): 1–15.

Arosio, P., Elia, L., and Poli, M., 2017. Ferritin, cellular iron storage and regulation. IUBMB Life 69(6): 414–422.

Blériot, C., Dupuis, T., Jouvion, G., Eberl, G., Disson, O., and Lecuit, M., 2015. Liver-Resident Macrophage Necroptosis Orchestrates Type 1 Microbicidal Inflammation and Type-2-Mediated Tissue Repair during Bacterial Infection. Immunity 42(1): 145–158.

Bolisetty, S., Zarjou, A., Hull, T. D., Traylor, A. M., Perianayagam, A., Joseph, R., Kamal, A. I., Arosio, P., Soares, M. P., Jeney, V., Balla, J., George, J. F., and Agarwal, A., 2015. Macrophage and epithelial cell H-ferritin expression regulates renal inflammation. Kidney international 88(1): 95–108.

Boring, L., Gosling, J., Chensue, S. W., Kunkel, S. L., Farese, R. V., Broxmeyer, H. E., and Charo, I. F., 1997. Impaired monocyte migration and reduced type 1 (Th1) cytokine responses in C-C chemokine receptor 2 knockout mice. Journal of Clinical Investigation 100(10): 2552–2561.

Bradford, M. M., 1976. A rapid and sensitive method for the quantitation of microgram quantities of protein utilizing the principle of protein-dye binding. Analytical Biochemistry 72(1–2): 248–254.

Bruttger, J., Karram, K., Wörtge, S., Regen, T., Marini, F., Hoppmann, N., Klein, M., Blank, T., Yona, S., Wolf, Y., Mack, M., Pinteaux, E., Müller, W., Zipp, F., Binder, H., Bopp, T., Prinz, M., Jung, S., and Waisman, A., 2015. Genetic Cell Ablation Reveals Clusters of Local Self-Renewing Microglia in the Mammalian Central Nervous System. Immunity 43(1): 92–107.

Cardoso, V., Chesné, J., Ribeiro, H., García-Cassani, B., Carvalho, T., Bouchery, T., Shah, K., Barbosa-Morais, N. L., Harris, N., and Veiga-Fernandes, H., 2017. Neuronal regulation of type 2

innate lymphoid cells via neuromedin U. Nature 549(7671): 277–281.

Chen, T. T., Li, L., Chung, D.-H., Allen, C. D. C., Torti, S. V., Torti, F. M., Cyster, J. G., Chen, C.-Y., Brodsky, F. M., Niemi, E. C., Nakamura, M. C., Seaman, W. E., and Daws, M. R., 2005. TIM-2 is expressed on B cells and in liver and kidney and is a receptor for H-ferritin endocytosis. The Journal of Experimental Medicine 202(7): 955–965.

Clausen B.E, C.Burkhardt, Reith, W., Renkawitz, R., and Förster I, 2001. Conditional gene targeting in macrophage and granulocytes using LysMcre mice. Transgenic Research 96(October): 317–330.

Cohen, L. A., Gutierrez, L., Weiss, A., Leichtmann-Bardoogo, Y., Zhang, D. L., Crooks, D. R., Sougrat, R., Morgenstern, A., Galy, B., Hentze, M. W., Lazaro, F. J., Rouault, T. A., and Meyron-Holtz, E. G., 2010. Serum ferritin is derived primarily from macrophages through a nonclassical secretory pathway. Blood 116(9): 1574–1584.

Corna, G., Caserta, I., Monno, A., Apostoli, P., Manfredi, A. A., Camaschella, C., and Rovere-Querini, P., 2016. The Repair of Skeletal Muscle Requires Iron Recycling through Macrophage Ferroportin. The Journal of Immunology 197(5): 1914–1925.

Darshan, D., Vanoaica, L., Richman, L., Beermann, F., and Kühn, L. C., 2009. Conditional deletion of ferritin H in mice induces loss of iron storage and liver damage. Hepatology 50(3): 852–860.

Datz, C., Müller, E., and Aigner, E., 2017. Iron overload and non-alcoholic fatty liver disease. Minerva Endocrinologica 42(2): 173–183.

De Domenico, I., McVey Ward, D., and Kaplan, J., 2008. Regulation of iron acquisition and storage: consequences for iron-linked disorders. Nature Reviews Molecular Cell Biology 9(1): 72–81.

Ferreira, C., Bucchini, D., Martin, M. E., Levi, S., Arosio, P., Grandchamp, B., and Beaumont, C., 2000. Early embryonic lethality of H ferritin gene deletion in mice. Journal of Biological Chemistry 275(5): 3021–3024.

Finazzi, D., and Arosio, P., 2014. Biology of ferritin in mammals: an update on iron storage, oxidative damage and neurodegeneration. Archives of toxicology 88(10): 1787–1802.

Frazer, D. M., and Anderson, G. J., 2014. The regulation of iron transport. BioFactors 40(2): 206–214.

Ganz, T., 2011. Hepcidin and iron regulation, 10 years later. Blood. 117(17): 4425–4433.

Ganz, T., 2012. Macrophages and systemic iron homeostasis. Journal of Innate Immunity 4(5–6):

446–453.

Ganz, T., and Nemeth, E., 2015. Iron homeostasis in host defence and inflammation. Nature Reviews Immunology 15(8): 500–510.

Gao, F., Lv, J., Wang, Y., Fan, R., Li, Q., Zhang, Z., and Wei, L., 2016. Tamoxifen induces hepatotoxicity and changes to hepatocyte morphology at the early stage of endocrinotherapy in mice. Biomedical Reports 4 102–106.

Geissmann, F., Jung, S., and Littman, D. R., 2003. Blood monocytes consist of two principal subsets with distinct migratory properties. Immunity 19(1): 71–82.

Gomez Perdiguero, E., Klapproth, K., Schulz, C., Busch, K., Azzoni, E., Crozet, L., Garner, H., Trouillet, C., de Bruijn, M. F., Geissmann, F., and Rodewald, H.-R., 2014. Tissue-resident macrophages originate from yolk-sac-derived erythro-myeloid progenitors. Nature 518(7540): 547–551.

Gozzelino, R., Andrade, B. B., Larsen, R., Luz, N. F., Vanoaica, L., Seixas, E., Coutinho, A., Cardoso, S., Rebelo, S., Poli, M., Barral-Netto, M., Darshan, D., Kühn, L. C., and Soares, M. P., 2012. Metabolic adaptation to tissue iron overload confers tolerance to malaria. Cell Host and Microbe 12(5): 693–704.

Gozzelino, R., Jeney, V., and Soares, M. P., 2010. Mechanisms of cell protection by heme oxygenase-1. Annual review of pharmacology and toxicology 50 323–354.

Gozzelino, R., and Soares, M. P., 2014. Coupling heme and iron metabolism via ferritin H chain. Antioxidants & redox signaling 20(11): 1754–1769.

Haldar, M., Kohyama, M., So, A. Y. L., Kc, W., Wu, X., Briseño, C. G., Satpathy, A. T., Kretzer, N. M., Arase, H., Rajasekaran, N. S., Wang, L., Egawa, T., Igarashi, K., Baltimore, D., Murphy, T. L., and Murphy, K. M., 2014. Heme-mediated SPI-C induction promotes monocyte differentiation into iron-recycling macrophages. Cell 156(6): 1223–1234.

Hasan, M. R., Koikawa, S., Kotani, S., Miyamoto, S., and Nakagawa, H., 2006. Ferritin forms dynamic oligomers to associate with microtubules in vivo: Implication for the role of microtubules in iron metabolism. Experimental Cell Research 312(11): 1950–1960.

Hashimoto, D., Chow, A., Noizat, C., Teo, P., Beasley, M. B., Leboeuf, M., Becker, C. D., See, P., Price, J., Lucas, D., Greter, M., Mortha, A., Boyer, S. W., Forsberg, E. C., Tanaka, M., van Rooijen, N., García-Sastre, A., Stanley, E. R., Ginhoux, F., Frenette, P. S., and Merad, M., 2013. Tissue-resident macrophages self-maintain locally throughout adult life with minimal contribution from circulating monocytes. Immunity 38(4): 792–804.

Hayashi, S., and McMahon, A. P., 2002. Efficient Recombination in Diverse Tissues by a Tamoxifen-Inducible Form of Cre: A Tool for Temporally Regulated Gene Activation/Inactivation in the Mouse. Developmental Biology 244(2): 305–318.

Hentze, M. W., Muckenthaler, M. U., Galy, B., and Camaschella, C., 2010. Two to Tango: Regulation of Mammalian Iron Metabolism. Cell 142(1): 24–38.

Hoeffel, G., Wang, Y., Greter, M., See, P., Teo, P., Malleret, B., Leboeuf, M., Low, D., Oller, G., Almeida, F., Choy, S. H. Y., Grisotto, M., Renia, L., Conway, S. J., Stanley, E. R., Chan, J. K. Y., Ng, L. G., Samokhvalov, I. M., Merad, M., and Ginhoux, F., 2012. Adult Langerhans cells derive predominantly from embryonic fetal liver monocytes with a minor contribution of yolk sac–derived macrophages. The Journal of Experimental Medicine 209(6): 1167–1181.

Holness, C. L., Da Silva, R. P., Fawcett, J., Gordon, S., and Simmons, D. L., 1993. Macrosialin, a mouse macrophage-restricted glycoprotein, is a member of the lamp/lgp family. Journal of Biological Chemistry 268(13): 9661–9666.

Huh, W. J., Khurana, S. S., Geahlen, J. H., Kohli, K., Waller, R. A., and Mills, J. C., 2012. Tamoxifen induces rapid, reversible atrophy, and metaplasia in mouse stomach. Gastroenterology 142(1):.

Hulsmans, M., Clauss, S., Xiao, L., Aguirre, A. D., King, K. R., Hanley, A., Hucker, W. J., Wülfers, E. M., Seemann, G., Courties, G., Iwamoto, Y., Sun, Y., Savol, A. J., Sager, H. B., Lavine, K. J., Fishbein, G. A., Capen, D. E., Da Silva, N., Miquerol, L., Wakimoto, H., Seidman, C. E., Seidman, J. G., Sadreyev, R. I., Naxerova, K., Mitchell, R. N., Brown, D., Libby, P., Weissleder, R., Swirski, F. K., Kohl, P., Vinegoni, C., Milan, D. J., Ellinor, P. T., and Nahrendorf, M., 2017. Macrophages Facilitate Electrical Conduction in the Heart. Cell 169(3): 510–522.e20.

Infante, A. A., Infante, D., Chan, M. C., How, P. C., Kutschera, W., Linhartová, I., Müllner, E. W., Wiche, G., and Propst, F., 2007. Ferritin associates with marginal band microtubules. Experimental Cell Research 313(8): 1602–1614.

Jinek, M., Chylinski, K., Fonfara, I., Hauer, M., Doudna, J. A., and Charpentier, E., 2012. A Programmable Dual-RNA – Guided DNA Endonuclease in Adaptice Bacterial Immunity. Science (New York, N.Y.) 337(August): 816–822.

Kautz, L., Jung, G., Valore, E. V, Rivella, S., Nemeth, E., and Ganz, T., 2014. Identification of erythroferrone as an erythroid regulator of iron metabolism. Nature Genetics 46(7): 678–684.

Kierdorf, K., Prinz, M., Geissmann, F., and Gomez Perdiguero, E., 2016. Development and function of tissue resident macrophages in mice. Seminars in Immunology 27(2015): 369–378.

Kohyama, M., Ise, W., Edelson, B. T., Wilker, P. R., Hildner, K., Mejia, C., Frazier, W. A.,

Murphy, T. L., and Murphy, K. M., 2009. Role for Spi-C in the development of red pulp macrophages and splenic iron homeostasis. Nature 457(7227): 318–321.

Kovtunovych, G., Ghosh, M. C., Ollivierre, W., Weitzel, R. P., Eckhaus, M. A., Tisdale, J. F., Yachie, A., and Rouault, T. A., 2014. Wild-type macrophages reverse disease in heme oxygenase 1-deficient mice. Blood 124(9): 1522–1530.

Kuhn, R., Schwenk, F., Aguet, M., and Rajewsky, K., 1995. Inducible gene targeting in mice. Science 269(5229): 1427–1429.

Kurotaki, D., Uede, T., and Tamura, T., 2015. Functions and development of red pulp macrophages. Microbiology and Immunology 59(2): 55–62.

Leimberg, M. J., Prus, E., Konijn, A. M., and Fibach, E., 2008. Macrophages function as a ferritin iron source for cultured human erythroid precursors. Journal of Cellular Biochemistry 103(4): 1211–1218.

Levi, S., Luzzago, A., Cesareni, G., Cozzi, A., Franceschinelli, F., Albertini, A., and Arosio, P., 1988. Mechanism of ferritin iron uptake: Activity of the H-chain and deletion mapping of the ferro-oxidase site. A study of iron uptake and ferro-oxidase activity of human liver, recombinant H-chain ferritins, and of two H-chain deletion mutants. Journal of Biological Chemistry 263(34): 18086–18092.

MacKenzie, E. L., Iwasaki, K., and Tsuji, Y., 2008. Intracellular iron transport and storage: from molecular mechanisms to health implications. Antioxid Redox Signal 10(6): 997–1030.

Mali, P., Yang, L., Esvelt, K. M., Aach, J., Guell, M., DiCarlo, J. E., Norville, J. E., and Church, G. M., 2013. RNA-Guided Human Genome Engineering via Cas9. Science 339(6121): 823–826.

McGrath, K. E., Frame, J. M., and Palis, J., 2015. Early hematopoiesis and macrophage development. Seminars in Immunology 27(6): 379–387.

Meyron-Holtz, E. G., Moshe-Belizowski, S., and Cohen, L. A., 2011. A possible role for secreted ferritin in tissue iron distribution. Journal of neural transmission (Vienna, Austria : 1996) 118(3): 337–347.

Muckenthaler, M. U., Rivella, S., Hentze, M. W., and Galy, B., 2017. A Red Carpet for Iron Metabolism. Cell 168(3): 344–361.

Muñoz, M., García-Erce, J. A., and Remacha, A. F., 2011. Disorders of iron metabolism. Part 1: molecular basis of iron homoeostasis. Journal of clinical pathology 64(4): 281–286.

Nahrendorf, M., and Swirski, F. K., 2016. Innate immune cells in ischaemic heart disease: Does myocardial infarction beget myocardial infarction?. European Heart Journal 37(11): 868–872.

Nairz, M., Theurl, I., Swirski, F. K., and Weiss, G., 2017. “Pumping iron”—how macrophages handle iron at the systemic, microenvironmental, and cellular levels. Pflugers Archiv European Journal of Physiology Pflügers Archiv - European Journal of Physiology 469(3–4): 397–418.

Nairz, M., Theurl, I., Wolf, D., and Weiss, G., 2016. Iron deficiency or anemia of inflammation?. Wiener Medizinische Wochenschrift 166(13–14): 411–423.

Papanikolaou, G., and Pantopoulos, K., 2017. Systemic iron homeostasis and erythropoiesis. IUBMB Life 69(6): 399–413.

Perdiguero, E. G., and Geissmann, F., 2015. The development and maintenance of resident macrophages. Nature Immunology 17(1): 2–8.

Pittet, M. J., Nahrendorf, M., and Swirski, F. K., 2014. The journey from stem cell to macrophage. Annals of the New York Academy of Sciences 1319(1): 1–18.

Samokhvalov, I. M., Samokhvalova, N. I., and Nishikawa, S., 2007. Cell tracing shows the contribution of the yolk sac to adult haematopoiesis. Nature 446(7139): 1056–1061.

Serbina, N. V, and Pamer, E. G., 2006. Monocyte emigration from bone marrow during bacterial infection requires signals mediated by chemokine receptor CCR2. Nature Immunology 7(3): 311–317.

Shi, S.-R., Shi, Y., and Taylor, C. R., 2011. Antigen retrieval immunohistochemistry: review and future prospects in research and diagnosis over two decades. The journal of histochemistry and cytochemistry : official journal of the Histochemistry Society 59(1): 13–32.

Sibille, J. C., Kondo, H., and Aisen, P., 1988. Interactions between isolated hepatocytes and kupffer cells in iron-metabolism - a possible role for ferritin as an iron carrier protein. Hepatology 8(2): 296–301.

Soares, M. P., and Hamza, I., 2016. Macrophages and Iron Metabolism. Immunity 44(3): 492–504.

Southern, J. a, Young, D. F., Heaney, F., Baumgartner, W. K., and Randall, R. E., 1991. Identification of an Epitope on the P-Proteins and V-Proteins of Simian-Virus 5 That Distinguishes between 2 Isolates with Different Biological Characteristics. Journal of General Virology 72(1991): 1551–1557.

Swirski, F. K., Nahrendorf, M., Etzrodt, M., Wildgruber, M., Panizzi, P., Figueiredo, J., Kohler, R. H., Chudnovskiy, A., Waterman, P., Aikawa, E., Mempel, T. R., Libby, P., Weissleder, R., and Pittet, J., 2009. Identification Monocytes Inflammatory of Splenic Reservoir and Their Deployment Sites. Science 325(5940): 612–616.

Theil, E. C., 2013. Ferritin: The protein nanocage and iron biomineral in health and in disease. Inorganic Chemistry 52(21): 12223–12233.

Theurl, I., Hilgendorf, I., Nairz, M., Tymoszuk, P., Haschka, D., Asshoff, M., He, S., Gerhardt, L. M. S., Holderried, T. A. W., Seifert, M., Sopper, S., Fenn, A. M., Anzai, A., Rattik, S., McAlpine, C., Theurl, M., Wieghofer, P., Iwamoto, Y., Weber, G. F., Harder, N. K., Chousterman, B. G., Arvedson, T. L., McKee, M., Wang, F., Lutz, O. M. D., Rezoagli, E., Babitt, J. L., Berra, L., Prinz, M., Nahrendorf, M., Weiss, G., Weissleder, R., Lin, H. Y., and Swirski, F. K., 2016. On-demand erythrocyte disposal and iron recycling requires transient macrophages in the liver. Nature Medicine 22(8): 945–951.

Torti, F. M., and Torti, S. V., 2002. Regulation of ferritin genes and protein. Blood 99(10): 3505–3516.

Tsou, C. L., Peters, W., Si, Y., Slaymaker, S., Aslanian, A. M., Weisberg, S. P., Mack, M., and Charo, I. F., 2007. Critical roles for CCR2 and MCP-3 in monocyte mobilization from bone marrow and recruitment to inflammatory sites. Journal of Clinical Investigation 117(4): 902–909.

Valny, M., Honsa, P., Kirdajova, D., Kamenik, Z., and Anderova, M., 2016. Tamoxifen in the Mouse Brain: Implications for Fate-Mapping Studies Using the Tamoxifen-Inducible Cre-loxP System. Frontiers in Cellular Neuroscience 10.

van Furth, R., 1976. ORIGIN AND KINETICS OF MONONUCLEAR PHAGOCYTES. Annals of the New York Academy of Sciences 278(1): 161–175.

Vanoaica, L., Darshan, D., Richman, L., Schümann, K., and Kühn, L. C., 2010. Intestinal ferritin H is required for an accurate control of iron absorption. Cell Metabolism 12(3): 273–282.

Varol, C., Mildner, A., and Jung, S., 2015. Macrophages: Development and Tissue Specialization. Annual Review of Immunology 33(1): 643–675.

Vooijs, M., Jonkers, J., and Berns, A., 2001. A highly efficient ligand-regulated Cre recombinase mouse line shows that LoxP recombination is position dependent. EMBO Reports 2(4): 292–297.

Wang, H., Yang, H., Shivalila, C. S., Dawlaty, M. M., Cheng, A. W., Zhang, F., and Jaenisch, R., 2013. One-step generation of mice carrying mutations in multiple genes by CRISPR/cas-mediated genome engineering. Cell 153(4): 910–918.

Wang, J., and Pantopoulos, K., 2011. Regulation of cellular iron metabolism. Biochemical Journal 434(3): 365–381.

Ward, R. J., Crichton, R. R., Taylor, D. L., Della Corte, L., Srai, S. K., and Dexter, D. T., 2011. Iron and the immune system. Journal of neural transmission (Vienna, Austria : 1996). 118(3):

315–328.

Weis, S., Carlos, A. R., Moita, M. R., Singh, S., Blankenhaus, B., Cardoso, S., Larsen, R., Rebelo, S., Schäuble, S., Del Barrio, L., Mithieux, G., Rajas, F., Lindig, S., Bauer, M., and Soares, M. P., 2017. Metabolic Adaptation Establishes Disease Tolerance to Sepsis. Cell 169(7): 1263–1275.e14.

Wilkinson, N., and Pantopoulos, K., 2014. The IRP/IRE system in vivo: Insights from mouse models. Frontiers in Pharmacology 5 JUL.

Yang, H., Wang, H., Shivalila, C. S., Cheng, A. W., Shi, L., and Jaenisch, R., 2013. Resource One-Step Generation of Mice Carrying Reporter and Conditional Alleles by CRISPR / Cas-Mediated Genome Engineering. Cell 154(6): 1370–1379.

Yona, S., Kim, K. W., Wolf, Y., Mildner, A., Varol, D., Breker, M., Strauss-Ayali, D., Viukov, S., Guilliams, M., Misharin, A., Hume, D. A., Perlman, H., Malissen, B., Zelzer, E., and Jung, S., 2013. Fate Mapping Reveals Origins and Dynamics of Monocytes and Tissue Macrophages under Homeostasis. Immunity 38(1): 79–91.

Yuan, X.-M., Li, W., Baird, S. K., Carlsson, M., and Melefors, O., 2004. Secretion of ferritin by iron-laden macrophages and influence of lipoproteins. Free radical research 38(10): 1133–1142.

Zhang, Y., and Orner, B. P., 2011. Self-assembly in the ferritin nano-cage protein superfamily. International Journal of Molecular Sciences 12(8): 5406–5421.

Zupančič, D., Terčelj, M., Štrus, B., and Veranič, P., 2017. How to obtain good morphology and antigen detection in the same tissue section?. Protoplasma 1–9.